Harmonic mechanical excitations of steady convective instabilities: a means to get more uniform heat transfers in mixed convection flows?

Xavier Nicolas, S. Mergui

Harmonic mechanical excitations of steady convective instabilities: a means to get more uniform heat transfers in mixed convection flows?

Xavier NICOLAS[1], Sophie MERGUI[2]

[1] Université Paris-Est, MSME UMR 8208 CNRS,
5 Boulevard Descartes, 77454 Marne la Vallée Cedex 2, France

[2] UPMC Université Paris 06, FAST UMR CNRS 7608,
Bat 502, Campus Universitaire, 91405 Orsay, France

Corresponding author: Xavier NICOLAS

Postal address: Université Paris-Est Marne-la-Vallée, Bât. Lavoisier,

MSME UMR 8208 CNRS, 5 Bd Descartes,

77454 Marne-la-Vallée Cedex 2, France.

Tel: [33] 1 60 95 73 14

Fax: [33] 1 60 95 72 94

E-mail: xavier.nicolas@univ-paris-est.fr

Other author e-mail: mergui@fast.u-psud.fr

Abstract

In laminar mixed convection flows, steady thermoconvective patterns generate non uniform heat and/or mass transfers at walls that can be detrimental in some industrial processes. For instance the longitudinal thermoconvective patterns of Poiseuille-Rayleigh-Bénard (PRB) flows generate non uniform thin films or coatings when they are present in cold wall horizontal Chemical Vapor Deposition (CVD) reactors. The aim of this paper is to show that, when the basic steady flow is convectively unstable against an unsteady flow regime, introducing small harmonic mechanical excitations in the basic flow may enable to obtain more uniform time averaged heat transfers. More specifically, three-dimensional direct

numerical simulations are used to characterize the temperature field and wall heat transfer associated with unsteady wavy convective instabilities of PRB flows that result from harmonic excitations of the longitudinal thermoconvective rolls at channel inlet. A design of experiments is used to build cubic response surfaces of the different quantities analyzed (growth length of the wavy rolls, magnitude of their spanwise oscillations, wall Nusselt number …) on a wide range of the flow parameters. Air PRB flows (Pr=0.71) in channels of aspect ratios equal to Width/Height=10 and $150 \leq$ Length/Height ≤ 300, for Reynolds numbers $100 \leq Re \leq 300$ and Rayleigh numbers $5000 \leq Ra \leq 16000$ are considered. Comparisons with experiments are presented and a good agreement is obtained. The optimal conditions to have uniform heat transfers on the horizontal walls of PRB flows correspond to the minimal growth length of the wavy rolls until saturation and the maximum magnitude of their spanwise oscillations. They are approximately obtained for moderate Reynolds number ($Re \approx 150$), high Rayleigh numbers ($Ra \approx 15000$), low excitation frequency and rather high excitation magnitude. A discussion of these results for the applications to CVD in horizontal rectangular reactors at atmospheric pressure is finally proposed.

1. Introduction

A Poiseuille-Rayleigh-Bénard (PRB) flow is a mixed convection flow in a horizontal rectangular channel heated from below and cooled from above. PRB flows are commonly encountered in industrial applications, for example in heat exchangers, during the air cooling of electronic circuit boards or in the rectangular Chemical Vapor Deposition (CVD) reactors used to make thin solid films or coatings on heated substrates from chemical precursors in gaseous phase (see [1, 2] for reviews). To optimize these industrial processes, heat and/or mass transfers at walls must be well controlled as well as the thermoconvective instabilities and the flow type (laminar, transitional, turbulent) that develop in the system. Indeed the thermoconvective instabilities can result in non uniform heat and mass transfers, especially when they are steady, and give rise to a degradation of the desired process (see [2-5] for instance in the case of CVD applications). It is then of great interest to characterize the flow patterns in the PRB configuration to enable a good controlling of the magnitude and homogeneity of heat and mass transfers.

In this paper, only laminar PRB flows are studied. The stable basic state is a purely conductive Poiseuille flow. Its successive destabilizations generate many different thermoconvective patterns, depending on the values of the characteristic parameters: the Reynolds, Re, Rayleigh, Ra, and Prandtl, Pr, numbers and the transverse aspect ratio of the channel, $B = W$ (width) / H (height). Thus the stability diagrams of PRB flows present many flow configurations. A few examples, established experimentally, theoretically and numerically, for different Prandtl numbers and aspect ratios, can be found in [6-9] in the case of pure fluids. In the case of air PRB flows (Pr=0.7), a complete stability diagram at $B \geq 10$ is presented in [10]. It is partially reproduced in Fig. 1 in order to specify the framework of the present study, in the next paragraphs. Very recently, Barletta and Nield [11] have analyzed the consequences of a uniform internal heat source on the thermal instability of the PRB mixed convection. Finally the stability of PRB flows in binary fluids, with and without Soret effect,

is studied in [12-15] for instance.

The primary instability made of steady parallel convection rolls oriented in the direction of the mean flow, referred to as longitudinal rolls, is the main flow pattern in all the stability diagrams of PRB flows at different Pr and B values (see Fig. 1). This instability is observed for sufficiently high Reynolds numbers (typically for Re>O(10) in air) and for Rayleigh numbers above a critical value varying between 1708 and 2000 when B>2 [9]. Carrière and Monkewitz (1999) [16] showed that this pattern is a convective instability of the basic conductive Poiseuille flow. Mergui et al. (2011) [17] and Benderradji et al. (2008) [18] demonstrated that these rolls are triggered in real channels of finite transverse aspect ratio just downstream the leading edge of the heated plate and near the vertical walls due to the presence of velocity and temperature boundary layers adjacent to these walls.
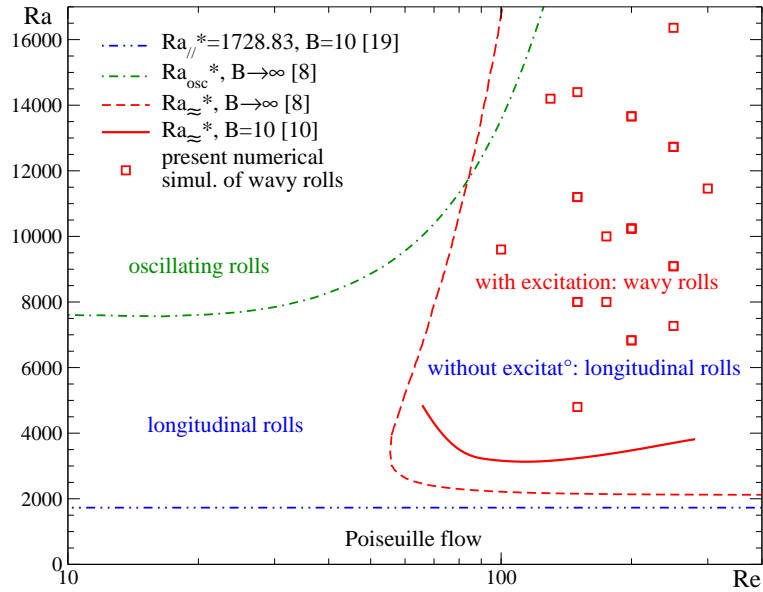
FIG. 1: Primary and secondary marginal stability curves of PRB flows at Pr=0.7 and B=10 or B→∞ determined by time linear stability analyses in [8, 10, 19]. $Ra_{//}*$ is the transition curve between the basic Poiseuille flow and the longitudinal rolls. $Ra_{osc}*(Re)$ and $Ra_{\approx}*(Re)$ are the transition curves between the longitudinal rolls and the oscillating and wavy rolls respectively. The simulation points of the wavy roll flows used in the present design of experiments are also indicated.

Two secondary unsteady instabilities appear at higher Rayleigh numbers, arising from

the destabilization of the longitudinal rolls. They are referred to as oscillating instabilities at low Reynolds number (Re<O(100)) and wavy instabilities at high Reynolds number (Re≥O(100)) (see Fig. 1). These instabilities have been first detected by Clever and Busse (1991) [8] through a time linear stability analysis for an infinite fluid layer. In the current paper, we focus on the wavy instability. The time linear stability analysis of longitudinal rolls against wavy rolls has been extended by Kato and Fujimura (2001) [20], Xin et al. (2006) [19] and Nicolas et al. (2012) [10] to channels of finite transverse aspect ratio. Previous experimental [21] and numerical [10, 22] studies showed that the wavy pattern can develop in the channel only if a perturbation is imposed and maintained into the longitudinal roll flow, meaning that the wavy rolls result from a convective instability of the longitudinal rolls.

This feature could be of great interest from a practical point of view. Indeed, the idea is to take advantage of the convective nature and unsteadiness of the wavy instability to enhance or weaken and/or homogenize the heat and/or mass transfers in the industrial processes by imposing the most appropriate perturbations/excitations to the flow. A numerical study by Nicolas et al. (2008) [2] has already shown that the presence of wavy rolls generated by harmonic mechanical excitations could homogenize the growth rate and the thickness of the deposited thin solid layers in APCVD (Atmospheric Pressure CVD) reactors. Nicolas et al. (2012) [10] conducted a numerical study to characterize the saturated wavy roll flows by maintaining a random excitation, a white noise on the transverse velocity components, at the channel inlet. It has been shown that, depending on the Reynolds and Rayleigh numbers and on the excitation amplitude, the spanwise displacement magnitude of the wavy rolls can be large on a large extent of the domain suggesting that this configuration could potentially be interesting to homogenize the heat and mass transfers in CVD reactors. However, in practical situations, a random excitation is almost impossible to implement and a sinusoidal perturbation will be preferred. Thus, the aim of the present study is to better characterize the spatial and temporal development of the wavy instability and of the associated heat transfers,

on a wide range of the control parameters, when a harmonic forcing is imposed to the system. The most effective conditions susceptible to homogenize the heat transfer at the channel walls and the main characteristics of the wavy roll flows (their growth length, the magnitude of the spanwise displacement of the oscillations, the wall Nusselt number at saturation, etc) will be numerically identified.

However, as the wavy roll flows are controlled by six parameters (Re, Ra, Pr, B and the magnitude, A_{exc}, and frequency, f_{exc}, of the harmonic forcing), the complexity of the problem is reduced by setting the values of Pr and B. More precisely, in all this work, Pr=0.71 (air flow) and B=10 to allow experimental and numerical comparisons with the PRB experiments carried out at FAST laboratory [17, 21, 23, 24]. Despite this simplification, the problem remains expensive to solve because one simulation of an unsteady fully-developed three-dimensional (3D) PRB flow requires channels of long streamwise aspect ratios (say A = L (length) / H ≈ 200), very large grids of more than 10^7 cells or nodes and, as a consequence, high computational resources. The computational cost of such simulations is presented for instance in [25] in the framework of a benchmark exercise on PRB flows, using different numerical methods on parallel or vectorial supercomputers. As the present study aims at analyzing the influence of four parameters (Ra, Re, A_{exc}, f_{exc}) on the wavy roll behavior, on a wide parameter domain, the total computational cost of the study could have been prohibitive. To overcome this difficulty, we decided to apply a design of experiments (DOE) [26]. This technique allows constructing polynomial interpolation surfaces of the studied quantities as a function of all the parameters, on the whole parameter domain, from a limited number of experiments (or simulations in the present case). The accuracy of the interpolation of course depends on the number and repartition of the simulations on the parameter domain and statistical tests are needed to determine it. This aspect will be discussed in the paper.

The paper is organized as follows. First, the mathematical model and the numerical methods are presented in §2. The way the design of experiments is built is presented in §3.

The methodology used and the definitions of the quantities (responses) analyzed to characterize the wavy roll flows are described in §4. The results are presented in §5. The wavy roll growth lengths until saturation and the magnitude of the most amplified modes at saturation are analyzed and compared with the experiments in §5.1 and §5.2. The magnitude of the spanwise oscillations of the wavy rolls and their spanwise wavelength are studied in §5.3. The optimum conditions for uniform time averaged heat transfers on the horizontal plates are determined in §5.4 and the intensity of these heat transfers at saturation are determined in §5.5. Finally, in §6, the main results of this study are summed up and discussed from the point of view of the possible applications to the horizontal rectangular CVD reactors. The statistical tests used to determine the accuracy of the response surfaces are presented in Appendix A. The equations of the response surfaces, not presented in the body of the text, are given in Appendix B and the values of the main responses are given in Appendix C for all the simulations of the DOE.

2. Mathematical model and numerical method

The channel considered to simulate the PRB flows is shown in Fig. 2. It is a horizontal rectangular channel of height H, width W and length L, heated from below. A fully developed Poiseuille flow enters into the channel at the cold temperature T_c, with an average velocity U_{mean}. After an adiabatic entrance zone of length L_e, the top wall is maintained at T_c and the bottom wall is heated at a higher temperature T_h. The vertical lateral walls are adiabatic all along the channel. The origin of the reference frame being placed at the beginning of the heated plate, the computational domain is defined by $(x, y, z) \in [-A_e, A-A_e] \times [0, B] \times [0, 1]$ in dimensionless Cartesian coordinates, where $A=L/H$ and $B=W/H$ are the streamwise and spanwise aspect ratios of the channel and $A_e=L_e/H$ is the streamwise entrance aspect ratio. In this study, $B = 10$, $A_e = 1$ and A varies between 150 and 300. Note that the ratio U_{max}/U_{meam} of the maximum and average Poiseuille velocities in a channel of B=10 is equal to 1.6009 [9].
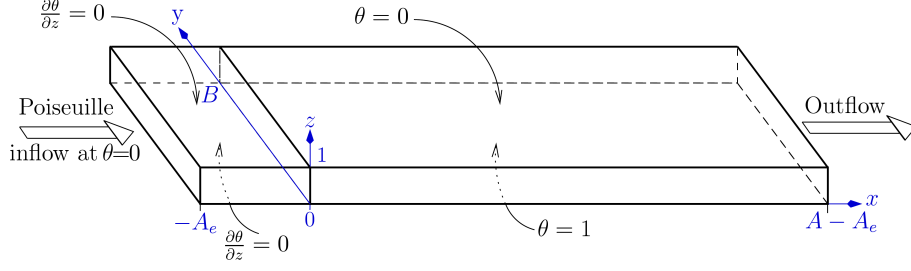
7

FIG. 2: Dimensionless geometry and thermal boundary conditions. The vertical lateral walls at y=0 and B are adiabatic all along the channel.

We consider PRB flows of an incompressible Newtonian fluid, governed by the 3D Navier-Stokes equations under the Boussinesq approximation. As already discussed in [2], this assumption is justified on the basis of the works by Chiu et al. (2000) [27] and Wang et al. (2003) [28] that show that the flow structure and the heat and mass transfers are little modified when the variations of the physical properties with temperature are not taken into account in simulations of CVD reactors with high temperature differences. Furthermore, the present simulations will be compared with FAST experiments [17, 21, 23, 24] in which the maximum temperature difference, T_h-T_c, in air flows is 40°C at Ra=10^4. Thus giving the reference quantities H, U_{mean}, ρU_{mean}^2, and H/U_{mean}, for the lengths, velocity, pressure and time respectively, and defining the reduced temperature θ=(T-T_c)/(T_h-T_c), the dimensionless governing equations for continuity, momentum and energy read as follows:

$$\nabla.\vec{v} = 0 \tag{1}$$

$$\frac{\partial \vec{v}}{\partial t} + (\vec{v}.\nabla)\vec{v} = -\nabla p + \frac{1}{Re}\nabla^2\vec{v} + \frac{Ra}{Re^2 Pr}\theta\vec{k} \tag{2}$$

$$\frac{\partial \theta}{\partial t} + \vec{v}.\nabla\theta = \frac{1}{Re\,Pr}\nabla^2\theta \tag{3}$$

where $\vec{v} = (u, v, w)$ is the dimensionless velocity vector, $\vec{k}$ the upward unit vector and p the deviation of the mixture pressure from the hydrostatic pressure. Ra=gβ(T_h-T_c)H^3/($\nu\alpha$), Re= U_{mean}H/ν and Pr=ν/α where g, β, ν and α are the gravity acceleration, the thermal expansion

coefficient, the kinematic viscosity and the thermal diffusivity respectively. The boundary conditions are:

at x=-A_e, u=u_{Pois}(y,z), v=0 $\forall$z or v=A_{exc}×2$\pi$$f_{exc}$×cos(2$\pi$$f_{exc}$t) at z=0.5, w=0, θ=0 (4)

at y=0 and B, $\vec{v} = \vec{0}$, $\partial\theta / \partial y = 0$ (5)

at z=0 and 1, for x∈[-A_e,0], $\vec{v} = \vec{0}$, $\partial\theta / \partial z = 0$ (6)

at z=1, for x∈[0, A-A_e], $\vec{v} = \vec{0}$, θ=0 (7)

at z=0, for x∈[0, A-A_e], $\vec{v} = \vec{0}$, θ=1 (8)

at x=A-A_e, $\partial f / \partial t + \partial f / \partial x = 0$ for f=u, v, w and θ (9)

In equation (4), the analytical expression of the Poiseuille profile, u_{Pois}(y,z), at the inlet is given in [9] and details of its numerical implementation are given in [25]. In this paper, to simulate the wavy rolls, a permanent sinusoidal excitation is introduced on the transversal velocity component, v, at mid-height of the inlet Poiseuille profile to approximately simulate the transverse oscillations of the horizontal rod placed at the entrance of the experimental channel [17, 23, 24]. This condition on v reads: at x=-A_e, $\forall$y∈[0, B] and $\forall$z∈[0, 1] v=0, except at z=0.5 where v=A_{exc}×2$\pi$$f_{exc}$×cos(2$\pi$$f_{exc}$t) with f_{exc} the excitation dimensionless frequency and 2A_{exc} the crest to crest dimensionless magnitude of the rod spanwise displacement (the reference frequency and displacement magnitude are U_{mean}/H and H, respectively). At the outlet (Eq. (9)), Orlanski type boundary conditions are used with a dimensionless average transport velocity u=1.

The problem (1-9) is solved using a finite difference method optimized for vectorial computers [22]. The equations are discretized in space on uniform, Cartesian and staggered grids using a centered scheme. The second-order Adams-Bashforth scheme is used for the time discretization. The dimensionless cell sizes and time step are Δx×Δy×Δz=0.1×0.055×0.029 and Δt=0.01. The time integration and the velocity-pressure coupling are solved by a projection method based on Goda's algorithm. The Helmholtz

equations for the temperature field and the components of the predicted velocity field are solved using an incremental factorization method of ADI type which permits to keep a second order time accuracy. The Poisson equation for the pressure increment is solved by a direct factorization method. The linear systems resulting from these two factorization methods are all tridiagonal and are solved by the TDMA algorithm. A detailed description of this code, its performances and several validations can be found in [10, 22, 25].

3. Building of the design of experiments

3.1. Choice of the factors and study domain

The quantities analyzed in a design of experiments (DOE) are usually called the "responses". They are interpolated with polynomials functions, called the "response surfaces", depending on the parameters of the problem called the "factors". The portion of the parameter domain limited by the minimum and maximum values of the range of each factor is called the "study domain". A very important step of a DOE is to adequately choose the factors and the study domain according to the responses that have to be analyzed.

At the beginning of the present study, it was decided to characterize the wavy roll flows using a four factor Doehlert design. It is a conventional DOE of 21 experiments (simulations) that enables to build quadratic response surfaces from a hexagonal distribution of the simulation points in the parameter domain [26]. However, it appeared that this DOE had to be modified due to a too much extended study domain and the lack of fit of the computed response surfaces. At large excitation magnitude, flows with ten or twelve wavy rolls were observed (a similar behavior is analyzed in [17, 19] for longitudinal roll flows) and, at low excitation frequency, the first harmonic of the excitation frequency was amplified by the flow, instead of its fundamental mode (a similar behavior is also observed experimentally in [23, 24]). In other words, different populations of wavy rolls were present in this study domain, generating strongly non linear behaviors of the responses, impossible to interpolate with

10

quadric or even cubic polynomials.

It was then decided to reduce the study domain and to analyze the wavy roll flows using a non conventional DOE of 31 simulations, enabling to compute cubic response surfaces, on the following parameter ranges: for Pr=0.7, B=10, $100 \leq Re \leq 300$ ($\Leftrightarrow$ $1.4 \leq Re/Re^* \leq 3.9$), $0.5 \leq \varepsilon \leq 3.5$ ($\Leftrightarrow$ $4800 \leq Ra \leq 16300$), $0.125 \leq f_{exc} \leq 0.3$ and $-0.387 \leq Log(A_{exc}) \leq 0.301$ ($\Leftrightarrow$ $0.41 \leq A_{exc} \leq 2$). Here $Re^* \approx 70 \pm 30$ is the critical Reynolds number between the longitudinal and wavy rolls that is the "vertical" part of the curve $Ra_{\approx}^*(Re)$ in Fig. 1. The parameter $\varepsilon = (Ra - Ra_{\approx}^*(Re))/Ra_{\approx}^*(Re)$ is the relative distance to the critical Rayleigh number, $Ra_{\approx}^*(Re)$, between the longitudinal and wavy rolls determined by a linear stability analysis [8, 10]. $Ra_{\approx}^*(Re)$ is drawn in Fig. 1 at Pr=0.7 for B=10 and B→∞. It can be seen that $3100 < Ra_{\approx}^*(Re) < 3900$ when $100 \leq Re \leq 300$ at B=10. The coordinates of the 31 simulation points of the DOE are given in Table 1 and their distribution in the study domain is presented in Fig. 3 (see also Fig. 1).
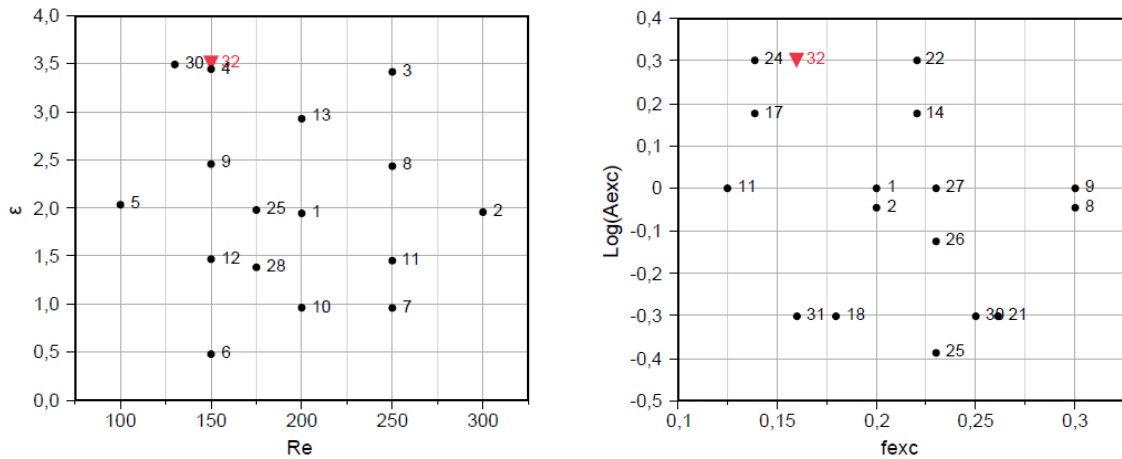

FIG. 3: Distribution of the DOE simulation points in the planes (ε, Re) and ($Log(A_{exc})$, f_{exc}). The numbers correspond to the cases given in Table 1. Some of the points of Table 1 are not shown because they are superimposed to others.

In the present DOE, the factor ε is preferred to Ra because it is well known that the main characteristics of the thermoconvective patterns in natural and mixed convection are related to ε (see [1, 8, 16, 29] for instance in mixed convection flows). The Reynolds number

range, 100≤Re≤300, was chosen, on the one hand, to avoid to be too close to the critical threshold between the longitudinal and wavy rolls at Re*≈70±30 and, on the other hand, to avoid too long wavy roll growth length, L_g, beyond Re>300, since L_g increases a lot when Re increases [10]. Furthermore, this Reynolds number range partly covers the one of the APCVD reactors envisaged as application of the present study since in these reactors $O(10) \leq Re \leq O(10^3)$ [2]. The chosen Rayleigh number range, 4800≤Ra≤16300, covers the whole domain studied in the experiments [17, 21, 23, 24] and a part of that covered by the APCVD applications. Indeed, Ra varies between $O(10^3)$ and $O(10^6)$ according to the temperature levels and the carrier gas used in the APCVD reactors [2]. The excitation frequency range, $0.125 \leq f_{exc} \leq 0.3$, was chosen in accordance with the results obtained when wavy roll flows are generated with a white noise imposed at channel inlet: in this case, the most amplified wavy roll modes are indeed observed for $0.18 \leq f_{exc} \leq 0.28$ [10]. Finally the excitation magnitude range, $0.41 \leq A_{exc} \leq 2$, corresponds to a maximum spanwise displacement of the inlet agitator that varies between 0.82H and 4H and it covers a part of the range of excitation magnitudes used in the experiments ($0.14 \leq A_{exc} \leq 1$). In the DOE, the considered factor is not A_{exc} but $Log(A_{exc})$ because it was shown in [10, 29] that the growth length of the wavy and transversal rolls in the PRB flows linearly decreases as a function of $Log(A_{exc})$.

3.2. Form of the response surfaces

In the present DOE, the response surfaces, noted $y(x_i)$, are looked for in the form of cubic polynomials as a function of the four factors x_i (i=1 to 4), with x_1=Re (or Re/Re*), x_2=ε, x_3=f_{exc} and x_4=$Log(A_{exc})$. They are thus written in the form:

$$y(x_i)=a_0+a_1x_1+a_2x_2+a_3x_3+a_4x_4+a_{12}x_1x_2+a_{13}x_1x_3+a_{14}x_1x_4+a_{23}x_2x_3+a_{24}x_2x_4+a_{34}x_3x_4$$

$$+a_{11}x_1{}^2+a_{22}x_2{}^2+a_{33}x_3{}^2+a_{44}x_4{}^2+a_{111}x_1{}^3+a_{222}x_2{}^3+a_{333}x_3{}^3+a_{444}x_4{}^3 \tag{10}$$

The 19 unknown coefficients a_i, a_{ij} and a_{iii} (i, j=1 to 4) of this cubic response surface are computed by a least square method knowing the values of the responses on the 31 simulation

points of the DOE (these values are partly provided in Table 3 of Appendix C). Note that, for the response surface given by Eq. (10) and the 31 points of the DOE, it was checked that the prediction variance function is lower than one in most of the study domain (see Appendix A).

TAB. 1. Parameters of the 31 simulation points used in the present DOE. Case #32 is not included in the DOE: it is the optimal point resulting from the analysis of § 5.4.

Case #	Re	Re/Re*	Ra	ε	f_{exc}	A_{exc}	A=L/H
1	200	2,72	10240	1,95	0,2	1	200
2	300	3,87	11460	1,96	0,2	0,9	200
3	250	2,70	16360	3,42	0,2	0,9	200
4	150	1,73	14400	3,45	0,2	1	200
5	100	1,40	9600	2,04	0,2	1	200
6	150	2,27	4800	0,48	0,2	1	300
7	250	3,93	7270	0,96	0,2	1	200
8	250	3,06	12730	2,44	0,3	0,9	200
9	150	1,96	11200	2,46	0,3	1	200
10	200	3,23	6830	0,97	0,3	1	250
11	250	3,58	9090	1,45	0,125	1	200
12	150	2,28	8000	1,47	0,125	1	200
13	200	2,37	13660	2,93	0,125	1	200
14	250	3,06	12730	2,44	0,2204	1,5	200
15	150	1,96	11200	2,46	0,2204	1,5	200
16	200	3,23	6830	0,97	0,2204	1,5	200
17	200	2,72	10240	1,95	0,1388	1,5	200
18	250	3,58	9090	1,45	0,1796	0,5	250
19	150	2,28	8000	1,47	0,1796	0,5	200
20	200	3,03	13660	2,93	0,1796	0,5	200
21	200	2,37	10240	1,95	0,2612	0,5	200
22	150	1,96	11200	2,46	0,2204	2	200
23	200	3,23	6830	0,97	0,2204	2	300
24	200	2,72	10240	1,95	0,1388	2	250
25	175	2,25	10000	1,98	0,23	0,41	200
26	175	2,25	10000	1,98	0,23	0,75	200
27	175	2,25	10000	1,98	0,23	1	200
28	175	2,66	8000	1,38	0,23	0,41	200
29	175	2,66	8000	1,38	0,23	0,75	200
30	130	1,51	14200	3,49	0,25	0,5	200
31	150	1,95	11300	2,49	0,16	0,5	150
32	*150*	*1,72*	*14575*	*3,50*	*0,17*	*2*	*150*

To estimate the relative influence of each factor on the studied responses and possibly simplify Eq. (10), centered and scaled factors x_i' (i=1 to 4) are used. They are defined as $x_i'=(x_i-x_{i,m})/\Delta x_i$, with $x_{i,m}=(x_{i,max}+x_{i,min})/2$ and $\Delta x_i=(x_{i,max}-x_{i,min})/2$, where $x_{i,max}$ and $x_{i,min}$ are the maximum and minimum values of the factor x_i on the study domain. Thus, on the whole study domain, the values of the four centered and scaled factors, x_i', vary between -1 and 1. As a consequence, it is possible to compare between themselves the values of the coefficients A_i, A_{ij} and A_{iii} of the modified Eq. (10), written as a function of x_i' instead of x_i, to determine the dominant factors. Furthermore, by comparing the value of a coefficient to its standard deviation, it is possible to simplify Eq. (10) by eliminating the negligible factors [26]. As a consequence, in §5 and Appendix B, only the simplified form of the response surface equations, written in terms of the normal factors x_i and in terms of the centered and scaled factors x_i', are presented. The various statistical tests used to characterize the quality of the interpolation by the response surfaces (the correlation coefficients, R^2 and R_a^2, and the Fisher test, F) and enabling to compute the 95% confidence interval of the responses are defined in Appendix A. In the result section (§5), whenever possible, the 95% confidence interval of a response is plotted in the figures and the numerical values of the responses are provided in the form "response value ± 95% confidence interval".

4. Methodology for the characterization of the wavy roll flows

In this section, the methodology used to simulate the wavy roll flows and the responses analyzed to characterize their space and time development and the associated heat transfers, are defined.

4.1. Main steps of the simulation procedure and signals recorded

Each simulation of a wavy roll flow is divided into three steps illustrated in Fig. 4: first, a longitudinal roll flow is simulated without any excitation, starting from a cold Poiseuille

14

flow as initial condition and imposing θ=1 at z=0, x∈ [0, A-A$_e$] for t>0. In the second step, the permanent sinusoidal excitation of v given by Eq. (4) is maintained in the inlet Poiseuille profile to trigger the wavy rolls and make them develop. This second step is a transient step that ends when fully developed wavy rolls are present in the whole channel. In the third step, the sinusoidal excitation is still maintained at the inlet and all the temperature and velocity time signals necessary to characterize the fully-developed wavy roll flows are recorded.
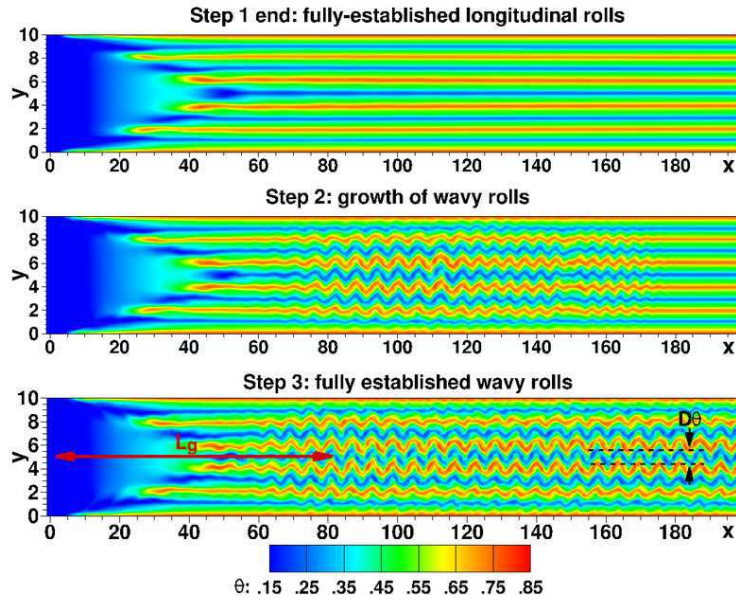
FIG. 4: Temperature field in the horizontal median plane at z=0.5, during the three steps of the establishment of ten wavy rolls in the DOE case #1 (see Table 1). The flow is from left to right and the unsteady waves travel in this direction. In blue is the cold entering and descending flow and in red is the hot ascending flow. In step 3, the wavy roll growth length, L$_g$, and the magnitude of their spanwise oscillations, Dθ, are depicted.

θ and v are recorded at each time step, during 26,000 to 30,000 iterations, all along the streamwise lines at (y, z)=(B/2, 0.5) and (B/2-1/3, 0.5) and the spanwise line at (x, z)=(A-A$_e$-30, 0.5). These time signals are analyzed through discrete Fourier transforms (DFT) to determine the space variation of the Fourier spectra in the wavy roll flows. The DFT are always performed on signals whose duration is a multiple of the period of the fundamental mode of the considered signal. Thus, it can be shown that the peak magnitudes, A(f$_i$), of the amplified

15

modes, f_i (i=1, 2, 3, …), in the Fourier spectra presented in this paper are equal to a quarter of the crest to crest amplitude of each mode in the Fourier decomposition of the recorded signals. Since the time step in the simulations is $\Delta t=0.01$ and the dimensionless recording duration is $t_{max}=260$ to 300, the highest frequency, f_{max}, and the frequency step, Δf, of the Fourier spectra are: $f_{max}=1/(2\Delta t)=50$ and $\Delta f=1/t_{max}\leq3.85\times10^{-3}$. As the excitation frequency and the fundamental frequencies in the Fourier spectra vary between 0.125 and 0.3, the recorded signals contain at least 37 periods and one period comprises at minimum 330 time steps. We have checked that this is enough to provide a Fourier analysis independent on Δt and the time signal duration.

4.2. Definition of the analyzed responses

In the present DOE, 31 wavy roll simulations are used to analyze around ten responses and build the corresponding response surfaces. These responses are defined now in the DOE case #1 because it is representative of all the other DOE cases since it is located in the middle of the studied parameter domain (see §3.1 and Fig. 3).

The first responses concern the space development of the wavy rolls that qualitatively occurs according to the same scenario whatever the case considered in the DOE. Fig. 5 presents an instantaneous signal and the envelope of the spanwise velocity component, v, along the channel axis, at (y, z) = (B/2, 0.5). This velocity component is equal to zero all along the axis for the longitudinal roll flows because an even roll number always develop and the channel axis is located between two longitudinal rolls. On the other hand, v is non-zero with wavy roll flows due to the spanwise oscillations generated by the inlet excitation. The envelope of v is computed by recording the maximum v values at each point of the channel axis throughout the entire step 3 of the simulation. The envelope of v at saturation is slightly modulated in the streamwise direction (see Fig. 5). Its average value in x direction is a constant denoted by V_s. For each simulation, the wavy roll growth length, L_g, is defined as the

first x position at which the envelope reaches V_s. The fully-developed wavy roll zone is defined as the zone where $x>L_g$. As illustrated in Fig. 5, the envelope magnitude strongly diminishes from the inlet (where $A_{exc}=1$ is imposed; see Table 1) to $x = 42$ in the DOE case #1. As shown in Fig. 4, this zone is the well known forced convection triangular zone [10, 17] where the longitudinal rolls develop from the lateral boundaries. For $42 \leq x \leq L_g=82$, the wavy roll spanwise oscillations grow to reach saturation and $V_s=0.23$ at $x=L_g$.
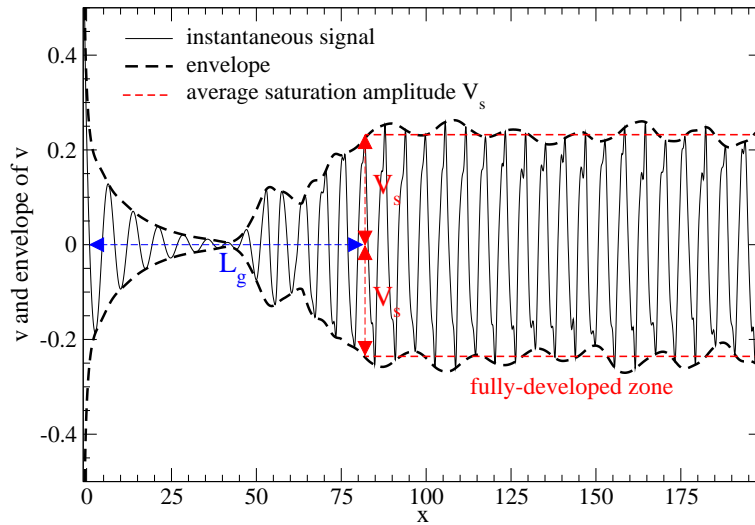
FIG. 5: Instantaneous signal and envelope of the spanwise velocity component, v, along the channel axis at (y, z) = (5, 0.5) for the DOE case #1 (recorded during step 3 of Fig. 4). The average saturation magnitude, V_s, and growth length, L_g, are depicted by double arrows.

In the experiments presented in [23, 24] with which comparisons are proposed in §5.1 and 5.2, only temperature time signals, $\theta(t)$, measured with micro thermocouples in numerous points of the channel, are used to characterize the space and time evolutions of PRB flows (velocities are not available). More precisely, the space development of the wavy rolls is analyzed thanks to the axial evolution of the $\theta(t)$ Fourier spectra. In the numerical simulations, both the $\theta(t)$ and spanwise velocity (v(t)) Fourier spectra are determined along channel axis at y=B/2 and B/2-0.33 and at z=0.5. In the development zone of the wavy rolls (for $0 \leq x \leq L_g=82$ for case #1; see Figs. 4 and 5), the magnitudes of the fundamental mode and harmonics globally increase with x. In the fully-developed zone, for $x>L_g=82$, the mode

magnitudes are nearly constant and up to fifteen harmonics appear in each spectrum. However the magnitudes of the four first modes, f_0 to f_3, are really of importance, the magnitudes of the remaining modes being at least one order smaller than the most amplified one. As illustrated in Fig. 6, the magnitudes $A_\theta(f_0)$, $A_\theta(f_1)$ and $A_\theta(f_2)$ of the three most amplified modes of the $\theta(t)$ signals slightly oscillate in the fully-developed zone, just as the v envelope displayed in Fig. 5. The average values over the range $x>L_g$ of the saturated magnitude are denoted by $\bar{A}_\theta(f_0)$, $\bar{A}_\theta(f_1)$ and $\bar{A}_\theta(f_2)$ and are depicted in Fig. 6. The growth lengths, $L_\theta(f_i)$, of each amplified mode ($i=0, 1, 2$) is defined as the first x position at which the magnitude of mode i reaches $\bar{A}_\theta(f_i)$. In case #1, $L_\theta(f_i)$ and L_g seems to be approximately equal since $L_\theta(f_i)$ ($i=0, 1,$ 2) varies between 83 and 86 (see Fig. 6) while $L_g=82$. It should also be mentioned that the mode magnitudes strongly vary with y as shown in Fig. 7 (and also with z; not shown here).
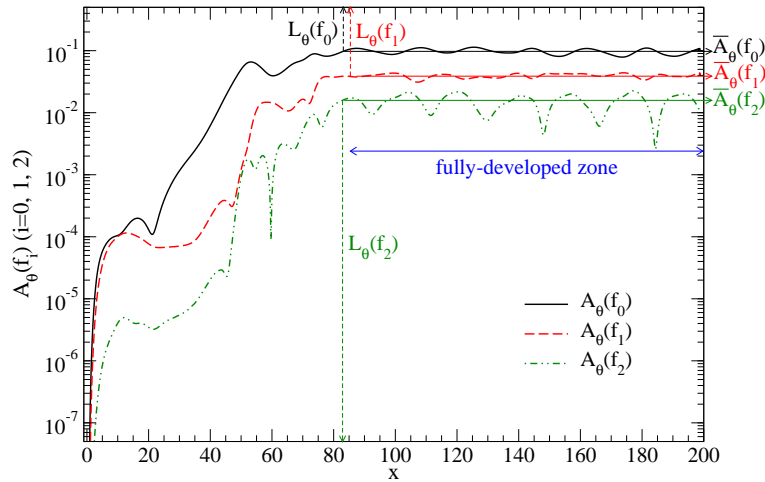

FIG. 6: Streamwise variation of the magnitude of the three first modes of the temperature signal, $\theta(t)$, near channel axis at (y, z) = (B/2-0.33, 0.5) for the DOE case #1. The growth lengths, $L_\theta(f_i)$, and the average magnitude at saturation, $\bar{A}_\theta(f_i)$ ($i=0, 1, 2$), of each mode are indicated.

The average magnitude of the spanwise displacement of the fully-developed wavy rolls at channel center is also analyzed by monitoring the position of the local minimum of the spanwise temperature profiles, $\theta(y)$, in the fully-developed region, at (x, z)=(A-30, 0.5), near

the channel center (for 4≤y≤6). This minimum corresponds to the cold downwards flow coming from the top plate and thus marks the boundary between the two rolls at channel center. For the wavy pattern, the position of this minimum at constant streamwise and vertical coordinates oscillates in the spanwise direction. We denote by $D\theta$ the average magnitude of these oscillations in the fully developed region. Details on the way $D\theta$ is computed are given in [10]. From the view point of CVD applications, it is interesting to determine how $D\theta$ varies with respect to the flow parameters. Indeed, the larger the magnitude of the wavy roll spanwise displacement is the more uniform the time average of the thin solid coatings on the heated substrate is [2]. In fact, to allow a good leveling of the depositions in CVD reactors, it would be necessary that the spanwise displacement of the wavy rolls is at least equal to their spanwise wavelength. Thus, in §5.3, the spanwise wavelength, λ_y, of the two contra-rotative wavy rolls at channel center will be computed from the θ signals. More precisely, it will be computed from the $A_\theta(f_0)$ signals as it is illustrated in Fig. 7.
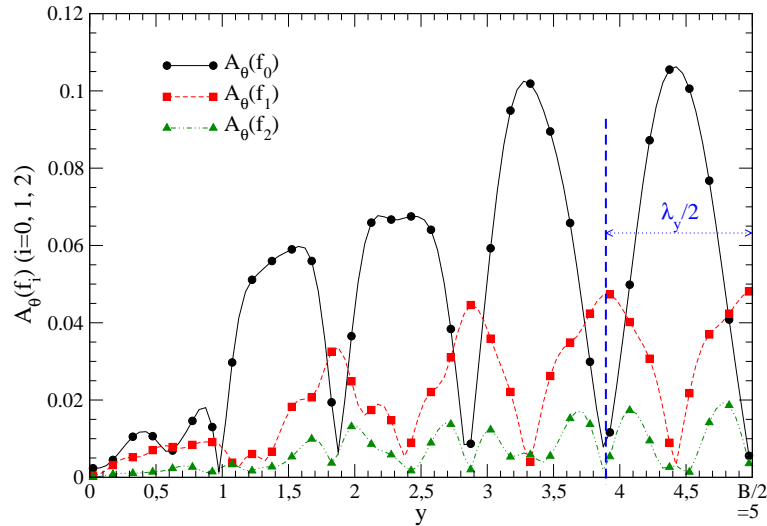

FIG. 7: Peak magnitude, $A_\theta(f_i)$ (i=1, 2, 3), of the three first modes of the temperature spectra at saturation, as a function of the spanwise coordinate y, at x=169 and z=0.5, obtained from direct numerical simulations at Re=175, Ra=10000, f_{exc}=0.23 and A_{exc}=0.75 (case #26 of Table 1). The determination of the spanwise wavelength, λ_y, of the wavy rolls at channel centre is illustrated.

Finally, to analyze the heat transfers on the bottom and top plates associated with PRB mixed convection, the local Nusselt number Nu(x; y; z=0, 1), the spanwise averaged Nusselt number $\overline{Nu}$ (x; z=0 or 1) and the averaged Nusselt number in the fully-developed region, $\overline{\overline{Nu}}_{fd}(z=0,1)$, are defined as:

$$Nu(x; y; z = 0, 1) = \left.\frac{\partial\theta}{\partial z}\right|_{z=0,1} \tag{11}$$

$$\overline{Nu}(x; z = 0, 1) = \frac{1}{B}\int_{y=0}^{B} Nu(x; y; z = 0, 1)dy \tag{12}$$

$$\overline{\overline{Nu}}_{fd}(z = 0, 1) = \frac{1}{A - A_e - L_g^+}\int_{x=L_g^+}^{x=A-A_e}\overline{Nu}(x; z = 0, 1)dx \tag{13}$$

where L_g^+ is a dimensionless length larger than the growth length, L_g, of the wavy rolls. As the wavy roll flows are unsteady, the local Nusselt numbers oscillate in time. A Nusselt number averaged in time over the whole third step of the simulations, during which the wavy roll flow is fully-established, is thus defined as:

$$< Nu > (x; y; z = 0,1) = \frac{1}{\Delta t_{step3}}\int_{t=0}^{\Delta t_{step3}}\left.\frac{\partial\theta}{\partial z}\right|_{z=0,1}dt \tag{14}$$

where Δt_{step3} is the duration of third step of the simulation. As the Nusselt numbers (13) slightly oscillates in time, it is in addition averaged as is done in Eq. (14).

To sum up, the main quantities analyzed in the following, for which response surfaces will be computed and some of them compared with experimental results, are: the wavy roll growth length until saturation, L_g and $L_\theta(f_i)$ (i=0, 1), the average magnitude at saturation of the two first modes contained in the temperature signals, $\bar{A}_\theta(f_i)$ (i=0, 1), the spanwise displacement magnitude, $D\theta$, the spanwise wave length of the wavy rolls near channel center, λ_y, and the averaged Nusselt number in the fully-developed region, $\overline{\overline{Nu}}_{fd}$.

5. Results and comparison with experiments

5.1. Wavy roll growth length

The simplified equation of the response surface for the wavy roll growth length, L_g, writes as a function of the normal factors:

$$L_g = 526.9922 - 167.6567\,(Re/Re^*) - 151.7345\,\varepsilon - 469.8198\,f_{exc} + 156.2139\,Log(A_{exc}) +$$

$$21.41344\,(Re/Re^*)^2 + 22.54020\,\varepsilon^2 + 1833.512\,f_{exc}^2 + 28.22014\,(Re/Re^*)\,\varepsilon - 195.5463$$

$$f_{exc}\,\varepsilon - 34.33355\,Log(A_{exc})\,(Re/Re^*) - 40.84351\,Log(A_{exc})\,\varepsilon \qquad (15)$$

The same equation as a function of the centered and scaled factors writes:

$$L_g = 70.2649 + 5.073633\,(Re/Re^*)' - 40.26428\,\varepsilon' - 6.943345\,f_{exc}' - 5.65777\,Log(A_{exc})'$$

$$+ 34.38466\,(Re/Re^*)'^2 + 51.13193\,\varepsilon'^2 + 14.03783\,f_{exc}'^2 + 53.8599\,(Re/Re^*)'\,\varepsilon' -$$

$$25.77062\,f_{exc}'\,\varepsilon' - 14.97172\,Log(A_{exc})'\,(Re/Re^*)' - 21.16919\,Log(A_{exc})'\,\varepsilon' \qquad (16)$$

The statistical tests indicate that the interpolation quality is very good since the correlation coefficients are $R^2=0.981$ and $R_a^2=0.970$, the Fisher ratio is F=87.9 and the root mean square error is RMSE=4.87 for a mean equal to Mean=90.52 (see Appendix A).

The dominant coefficients of Eq. (16) are those of ε', $(Re/Re^*)'^2$, ε'^2 and of the interaction $(Re/Re^*)'\varepsilon'$. All the cubic terms, the quadratic term $Log(A_{exc})'^2$ and two interactions $((Re/Re^*)'f_{exc}'$ and $f_{exc}'Log(A_{exc})')$ are neglected because it was checked that the values of their coefficients are smaller than their standard deviation [26]. This indicates that, in the parameter domain under study, L_g mainly depends on ε and Re/Re^* and to a lesser extent on f_{exc} and A_{exc}. This is illustrated in Fig. 8 where L_g behavior is presented as a function of the four factors around the center of the study domain at point $Re/Re^*=2.5$, $\varepsilon=2.5$, $f_{exc}=0.2$ and $A_{exc}=1$. Around this point, one can see that L_g slightly decreases as f_{exc} or A_{exc} increases. This behavior has been observed in the whole study domain, except when Re/Re^* and ε are simultaneously small (typically for $Re/Re^*<1.5$ to 2 and $\varepsilon<1$ to 1.5): in this case, L_g increases as f_{exc} or A_{exc} increases.
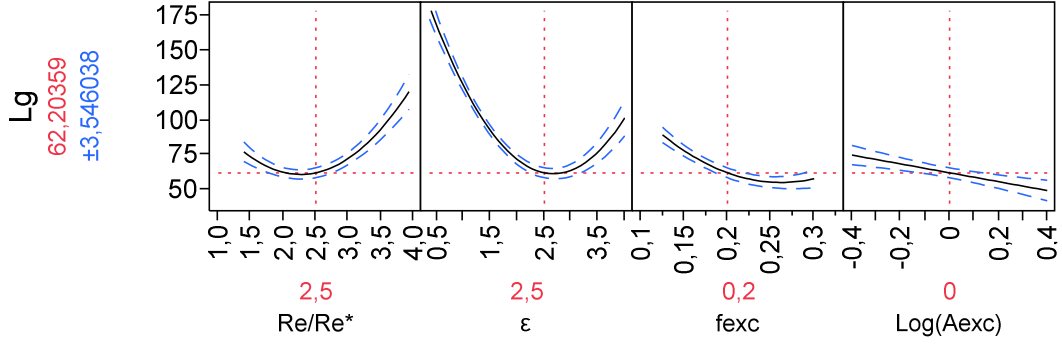
FIG. 8: Wavy roll growth length, L_g, as a function of four parameters Re/Re*, ε, f_{exc} and Log(A_{exc}). Each graph presents L_g as a function of one parameter, the three others being fixed at the value noted in red below each abscissa. The dashed blue lines indicate the 95% confidence interval. The L_g value is given in red, with its confidence interval in blue, near the ordinate axis for the four parameter values fixed at Re/Re*=2.5, ε=2.5, f_{exc}=0.2 and A_{exc}=1.

As described in §4.2, in the experiments at Fast laboratory [23], the wavy roll growth lengths (or saturation length) are measured from the streamwise variation of the mode magnitude of the temperature time signals recorded at y=B/2-0.33 and z=0.5. For the fundamental mode and its first harmonic, these growth lengths are denoted by $L_\theta(f_0)$ and $L_\theta(f_1)$, respectively. They are compared now with the values of L_g, $L_\theta(f_0)$ and $L_\theta(f_1)$ obtained by the numerical simulations and given by Eqs. (15-16) and, in Appendix B, by Eqs. (19-22). Fig. 9 compares the experimental and numerical values of $L_\theta(f_1)$ with respect to f_{exc} and A_{exc}, at Ra≈8000 and 10000 and Re≈175. It clearly appears that experiments and simulations are in good agreement and provide the same variations of $L_\theta(f_1)$ with respect to the flow parameters: $L_\theta(f_1)$ decreases when A_{exc} or Ra increases but varies very little with f_{exc} in the range $0.17 \leq f_{exc} \leq 0.27$. On the other hand, the experimental values of $L_\theta(f_1)$ are quasi systematically lower than the numerical values: the discrepancy is around 8 unities on average but it can be considered negligible considering that the uncertainty bars are often larger. The intrinsic background noise of the experimental apparatus could explain this discrepancy. Note that the experimental point at Ra=7900 (ε=1.35), Re=176 (Re/Re*=2.69), A_{exc}=1 and f_{exc}=0.26 is clearly below its numerical counterpart probably because the saturation zone of the wavy rolls is not fully reached in this experiment.
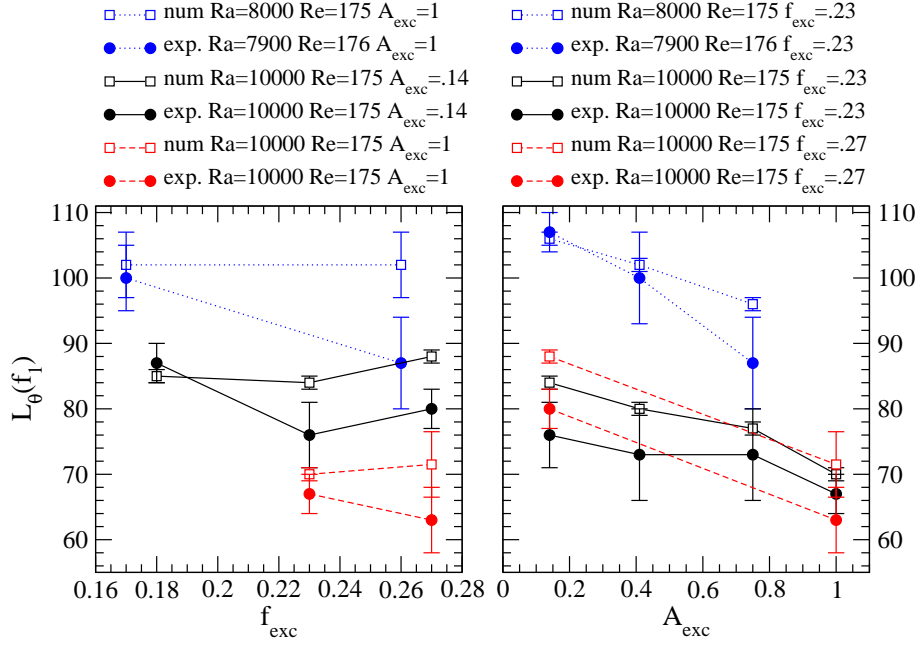
FIG. 9: Experimental [23] and numerical comparison of the wavy roll growth length until saturation, $L_\theta(f_1)$, with respect to f_{exc} and A_{exc}, at Ra≈8000 and 10000 and Re≈175. The numerical results are obtained by DNS, except when they are unavailable: in this case, the solution of the $L_\theta(f_1)$ response surface is used (cf. Table 2).

For more accuracy, Table 2 gives the values of $L_\theta(f_0)$, $L_\theta(f_1)$ and L_g obtained experimentally and numerically, including the values of Fig. 9. The numerical results comes either from the response surfaces of the DOE or directly from the numerical simulations (DNS). Note that $L_\theta(f_0)$ is very difficult to measure, particularly in the experiments, because the magnitude of the fundamental mode strongly oscillates. The relative discrepancy between the numerical and experimental results is generally smaller than 13% but can reach 17% for some cases. It appears that $L_\theta(f_0)$ is generally slightly smaller than $L_\theta(f_1)$. Moreover L_g is nearly equal to $L_\theta(f_1)$ and thus both the fluctuations of the temperature and velocity fields can be used to determine the growth length of the wavy rolls. Finally, it is also noteworthy that the results of the response surfaces (DOE) are always coherent with the results of the direct numerical simulations (DNS) when the confidence intervals and the error bars are taken into account.

Flow parameters				$L_\theta(f_0)$			$L_\theta(f_1)$			L_g		DOE case #
Ra ε	Re Re/Re*	A_{exc}	f_{exc}	exp.	DOE	DNS	exp.	DOE	DNS	DOE	DNS	
10000 1.98	175 2.4	1	0.27	60±7	67±5.5 *11%*		63±5	71.5±5 *13%*		72±4 *14%*		
		1	0.23	NA	64±4.5	71±2	67±3	69±4 *3%*	70±1 *4%*	70±3.5 *4%*	67±1 *0%*	27
		0.75	0.23	NA	68±4	74±2	73±7	70±4 *-4%*	77±1 *5%*	71±3.5 *-3%*	75±1 *3%*	26
		0.41	0.23	NA	75±6	80±2	73±7	73.5±6 *1%*	80±1 *9%*	73±4.5 *0%*	77±1 *5%*	25
		0.14	0.23	NA		84±2	76±5	*79±11* *4%*	84±1 *10%*	*76±8* *0%*	80±1 *5%*	
		0.14	0.18	80±7		85±4 *6%*	87±3		85±1 *-2%*	*81±8* *-7%*	89±1 *2%*	
		0.14	0.27	74±7		87±2 *16%*	80±3		88±1 *10%*	*78±9* *-2%*	84±1 *5%*	
7900 1.35	176 2.69	0.75	0.23	NA	98±5	96±2	87±7	99±4 *13%*	96±1 *10%*	97±3.5 *11%*	91±1 *4%*	29
		0.41	0.23	100±7	109±7 *9%*	101±2 *1%*	NA	103±7	102±1	94.5±6	97±1	28
		0.14	0.23	107±7		105±1 *-2%*	107±3		106±1 *-1%*		101±1 *-6%*	
		1	0.17	87±3	90.5±5 *4%*		100±5	102±5 *2%*		98±4 *-2%*		
		1	0.26	87±7	97±6.5 *11%*		87±7	102±5 *16%*		103±4 *17%*		

TAB. 2: Comparison of the wavy roll growth lengths, $L_\theta(f_0)$, $L_\theta(f_1)$ and L_g, obtained in experiments [23] and numerically from the response surfaces (DOE) or from simulations (DNS). In the second series of results, the DNS parameters are (Ra, ε, Re, Re/Re*) = (8000, 1.38, 175, 2.66) instead of (7900, 1.35, 176, 2.69) in the experiments and DOE. The percentages below the numerical results indicate the relative discrepancy with the experimental result except when it is not available (NA) due to the difficulty of measuring. For L_g, the discrepancies are computed with the experimental values of $L_\theta(f_1)$. Some DOE results are noted in italics because the response surfaces are solved outside the DOE study domain (cases at A_{exc}=0.14).

Fig. 10 displays isovalues of L_g and $L_\theta(f_1)$, computed from the response surfaces, in the plane (Re/Re*, ε) at f_{exc}=0.2 and A_{exc}=1. This figure confirms that the two growth lengths provide nearly the same information. It is noteworthy that wavy roll growth lengths smaller than 60 are reached at high Rayleigh numbers (for $\varepsilon\approx3$) and moderate Reynolds numbers (for Re/Re*≈2). In fact, in the study domain, the minimum growth length, according to Eq. (15), is L_g=23±18 at Re/Re*=1.85, ε=3.5, f_{exc}=0.3 and A_{exc}=2; while the minimum growth length according to Eq. (21) of Appendix B is $L_\theta(f_1)$=38±21 at Re/Re*=1.93, ε=3.26, f_{exc}=0.3 and

A_{exc}=2. From the viewpoint of CVD application, this means that fully established unsteady wavy roll flows and, as a consequence, better conditions to homogenize the heat and mass transfers can be obtained in the largest part of some CVD reactors [2].
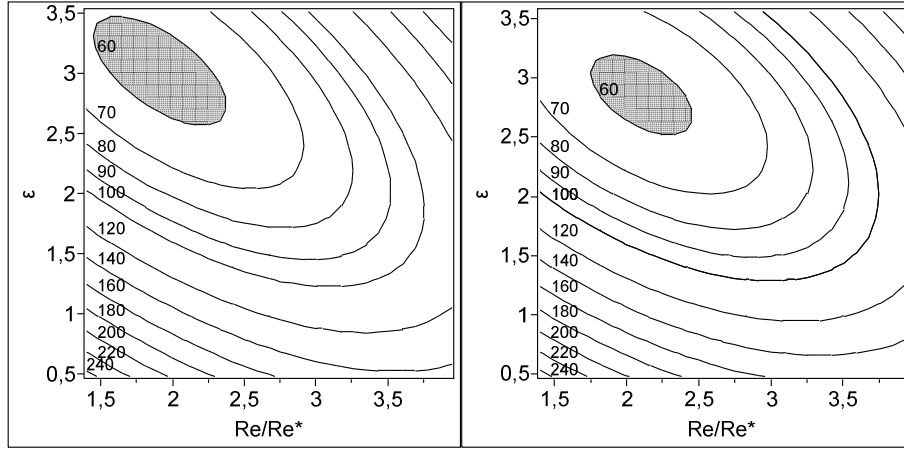

FIG. 10: Isovalues of L_g (on the left) and $L_\theta(f_1)$ (on the right) in the plane (Re/Re*, ε) for f_{exc}=0.2 and A_{exc}=1. The zone corresponding to wavy roll growth lengths smaller than 60 is colored in grey.

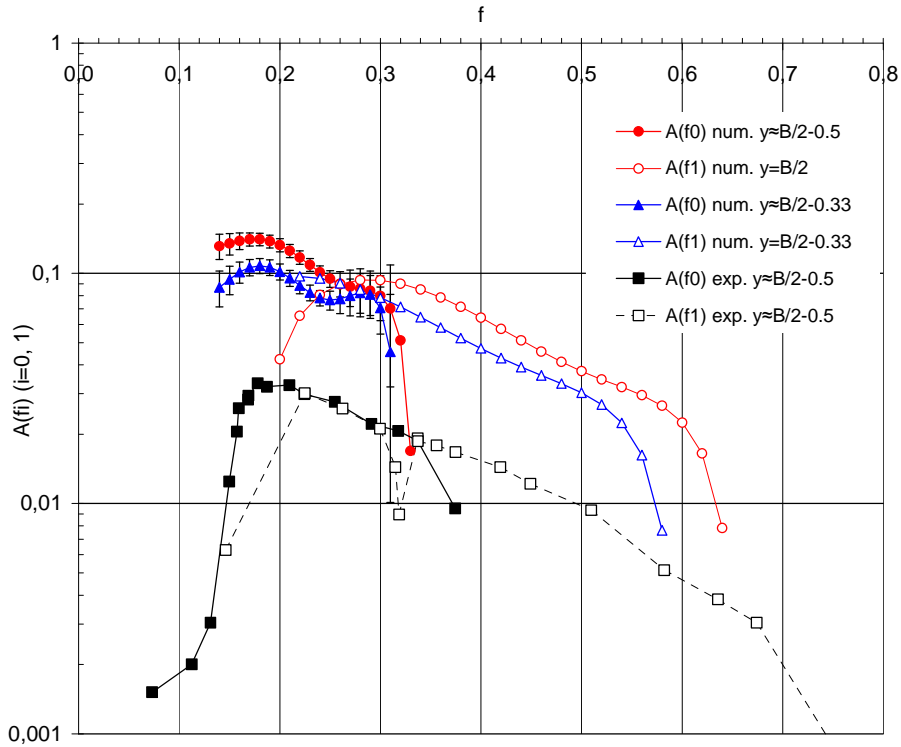### 5.2. Magnitude of the most amplified modes at saturation

Fig. 11 displays the averaged magnitude of the two first modes of the temperature spectra at saturation, $\bar{A}_\theta(f_0)$ and $\bar{A}_\theta(f_1)$ (defined in §4.2 and Fig. 6), as a function of the frequency at Re=175 (Re/Re*=2.4), Ra=10000 (ε=1.98) and A_{exc}=0.41, compared to experimental results presented in [24]. The temperature time signals are recorded at z=0.5 and different spanwise coordinates, y, nearby channel center. The results are plotted from the response surface Eqs. (23-30) of Appendix B. A close examination of the coefficients of these equations, based on centered and scaled factors, clearly indicates that $\bar{A}_\theta(f_i)$ (i=0, 1) strongly depend on Re, ε and f_{exc} on the studied parameter domain. On the other hand, as it could have been expected, they are very little dependent on A_{exc}.

Fig. 11 shows that the experimental and numerical results are qualitatively in very good agreement. Indeed the slopes of the curves $\bar{A}_\theta(f_i)$ are similar for i=0 and 1 whatever the spanwise coordinate of the monitoring point (y=B/2, B/2-0.33 and B/2-0.5). Furthermore, the

most amplified mode is detected for f≈0.18 numerically and for f=0.19±0.01 experimentally. This mode is smaller than the most amplified mode observed with random excitations in [10] (f°=0.23±0.02 for 150<Re<200, ε=2 and A_{exc}=0.1) and the mode with the maximum spatial growth rate observed in the experiments in the framework of the linear theory (f≈0.24 in [21] and f=0.22±0.02 at Re/Re*=2.4 and Ra=10000 in [24]).

FIG. 11: Numerical averaged magnitude of the two first modes in the temperature spectra at saturation, $\bar{A}_\theta(f_0)$ and $\bar{A}_\theta(f_1)$, as a function of frequency, for different spanwise coordinates y, at z=0.5, Re=175 (Re/Re*=2.4), Ra=10000 (ε=1.98) and A_{exc}=0.41. Comparison with experiments presented in [24]. The numerical results are obtained from the response surfaces given in Appendix B (Eqs. (23-30)); here they are slightly extended outside their validity domain defined by $0.15 \leq f_0 \leq 0.3$ and $0.25 \leq f_1 \leq 0.6$.

On the other hand, the magnitudes of the experimental and numerical curves in Fig. 11 are very different: there is nearly a factor four between them. This can probably be explained as follows. The coordinates of the probes that measure the temperature time signals and their relative positions in the convection rolls are exactly controlled in the numerical simulations but not in the experiments. Experimentally, the position of the thermocouples relative to a

convection roll is not controlled since the convection pattern of real PRB flows is never perfectly symmetric through the streamwise median vertical plane. As a consequence, the relative error on the spanwise position of the thermocouple is estimated to be around 20%. It has been shown in Fig. 7 that the spanwise variation of the mode magnitude $\bar{A}_\theta(f_i)$ is very important depending on the spanwise location of the monitoring point. Moreover, the vertical position of the monitoring point also influences the amplitude of the signal. Therefore a small error in the thermocouple location can provide a large error on the measurement of the mode magnitude. In the experiments, $\bar{A}_\theta(f_i)$ (i=0, 1) is approximately measured at y≈B/2-0.5 and z≈0.5. In the numerical simulations, $\bar{A}_\theta(f_1)$ is really measured at z=0.5 and y=B/2 or B/2-0.33 while $\bar{A}_\theta(f_0)$ is measured at z=0.5 but near y=B/2-0.5 or B/2-0.33. Indeed, the values of $\bar{A}_\theta(f_0)$ correspond in fact to the maximum of $\bar{A}_\theta(f_0)$, measured near y=B/2-0.5 (cf. Fig. 7) or to the values measured at y≈B/2-λ_y/6, where λ_y is the dimensionless spanwise wavelength of the two rolls at channel center which is approximately equal to 2. To a lesser extent, another explanation of the experimental and numerical discrepancies in the mode magnitudes observed in Fig. 11 could also be ascribed to the heat conduction in the Plexiglas top plate used in the experiments. This is not taken into account in the simulations but it is well known that conducting horizontal walls can modify the spanwise wavelength of the thermoconvective rolls [17, 30]. As a consequence, the magnitudes measured at the same point in the cases with perfectly and finitely conducting horizontal boundaries can be different for the same Rayleigh number value.

In Fig. 11, the modes denoted by f_0 correspond to the excitation modes. Experimentally, when the excitation frequency is low (f_{exc}<0.12), it clearly appears that the most amplified mode is the first harmonic, f_1=2f_0, instead of the fundamental mode, f_0. The DOE response surfaces of $\bar{A}_\theta(f_0)$ have been obtained for f_{exc}>0.125. They cannot reproduce the steep variation observed experimentally for 0.1<f_0<0.2 (even if quintic polynomials as a function of f_{exc} were used for these response surfaces: see Eqs. (23, 24, 27, 28) in Appendix B).

5.3. Spanwise oscillation magnitude and spanwise wavelength of wavy rolls

As already explained in §4.2 and demonstrated in [2], a large magnitude of the spanwise oscillations of the wavy rolls would be interesting from the view point of CVD applications to get a more uniform time average of the deposition thickness. In the present study, the spanwise displacement of wavy rolls is characterized by $D\theta$ defined in §4.2. The simplified response surfaces of $D\theta$ are given in Appendix B, Eqs. (31-32). As illustrated in Fig. 12 and already observed for $\bar{A}_\theta(f_i)$ (i=0, 1, 2) in §5.2, $D\theta$ depends very little on A_{exc} but strongly depends on f_{exc} and, to a lesser extent, on ε and Re: globally, $D\theta$ increases when f_{exc} and Re decrease and ε increases, but it remains constant for $\varepsilon \geq 2$.
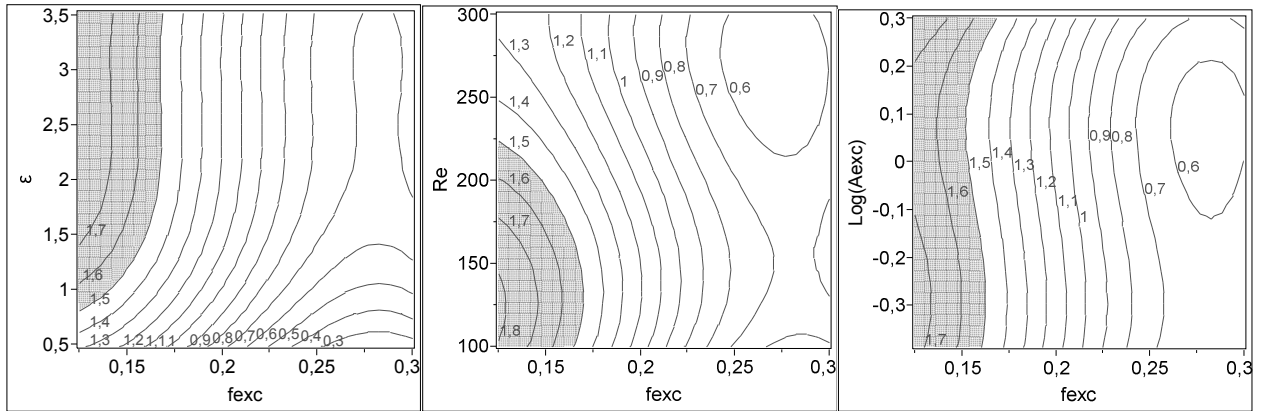
FIG. 12: Isovalues of the wavy roll spanwise displacement, $D\theta$, as a function of ε and f_{exc} at Re=150 and A_{exc}=2 (left), as a function of Re and f_{exc} at ε=2.5 and A_{exc}=2 (center), as a function of A_{exc} and f_{exc} at ε=2.5 and Re=150 (right). The shaded area indicates displacements greater than 1.5.

Fig. 12 shows that spanwise displacements $D\theta$ larger than 1.8 are possible. The response surface (Eq. (31)) indicates that the maximum spanwise displacement of the wavy rolls is $D\theta_{max}$=1.83±0.15 obtained at Re=125, ε=3.5, f_{exc}=0.125 and A_{exc}=2. This therefore means that $D\theta_{max}$ is just a little smaller than the dimensionless spanwise wavelength, λ_y, of the wavy rolls at channel center. Indeed, λ_y has been computed as defined in §4.2 and Fig. 7 for the 31 cases of the DOE (see Table 3 of Appendix 3) and its response surface is Eqs. (33-

34) in Appendix B. It indicates that λ_y varies between 1.55±0.09 and 2.82±0.10 in the studied parameter domain (see Fig. 13) and that its average value is equal to 2.18. At point Re=125, ε=3.5, f_{exc}=0.125 and A_{exc}=2, where $D\theta$=$D\theta_{max}$=1.83±0.15, the response surface provides λ_y = 2.33±0.08. As a consequence, more uniform heat transfers and a better leveling of the solid coatings produced in some APCVD reactors could be conceivable by making develop well amplified wavy roll flows. This suggestion is analyzed with more details in the next section.
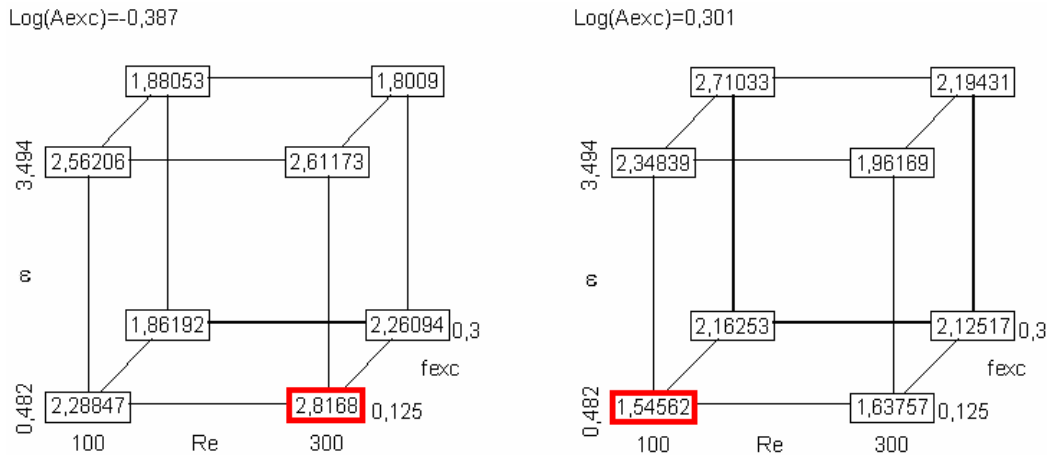
FIG. 13: Cube plots of the spanwise wavelength λ_y at A_{exc}=0.41 on the left and A_{exc}=2 on the right: the cubes display the values of the λ_y response surface (Eqs. (33-34)), laid out in rectangles on the cube vertices, for the extremes of the factor ranges ($100 \leq Re \leq 300$ on the horizontal axis, $0.482 \leq \varepsilon \leq 3.494$ on the vertical axis and $0.125 \leq f_{exc} \leq 0.3$ on the depth axis). The two red boxed λ_y values are the minimum and maximum values of λ_y in the study domain.

5.4. Optimum conditions for uniform heat transfers on the horizontal plates

In this section, we are going to determine the best values of the parameters Re, ε, f_{exc} and A_{exc} to get uniform heat transfers on the bottom plate of the PRB flows under study (for B=10 and Pr=0.7). These conditions will be satisfied if the growth length, L_g, of the fully-developed wavy rolls is as short as possible and the magnitude of their spanwise displacement, $D\theta$, is as large as possible. According to the previous discussions in §5.1 and 5.3, we decide that the sought objective is to simultaneously check L_g<60 and $D\theta$>1.5. In that aim, the full response surfaces of L_g and $D\theta$ (not simplified) are analyzed both together in

Figs. 14 for the largest values of ε and A_{exc} (ε=3.5 and A_{exc}=2). Indeed, Figures 8, 10 and 12 have shown that small values for L_g and large values for Dθ are simultaneously obtained when ε and A_{exc} are large. Figure 14 shows that Re and f_{exc} have antagonist effects on L_g and thus are more difficult to fix to satisfy the objective. The criteria L_g<60 and Dθ>1.5 are satisfied in a very restricted area around Re=155 and f_{exc}=0.17. Using the four parameter values (ε=3.5, A_{exc}=2, Re=155, f_{exc}=0.17) the results predicted by the response surfaces are: L_g=59.8±22.1 and Dθ=1.51±0.19. As the 95% confidence intervals are quite large, it is necessary to check whether the prediction is correct or not and whether uniform heat transfers are really observed for these parameter values.
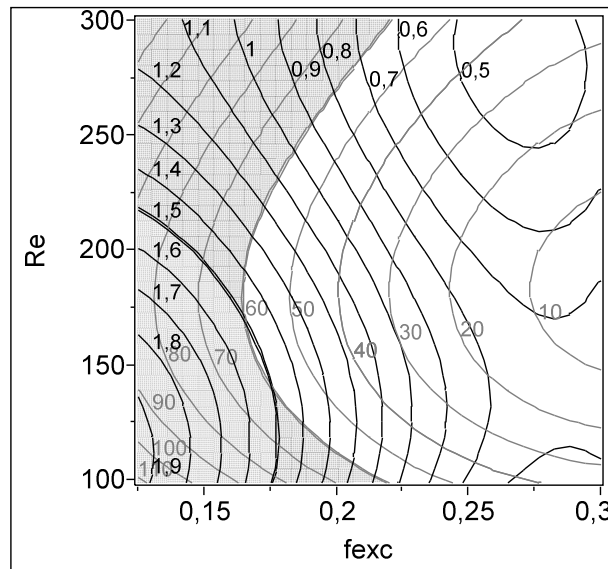
FIG. 14: Superimposition of the isovalues of L_g (gray lines) and Dθ (black lines) in the plane (Re, f_{exc}) for ε=3.5 and A_{exc}=2. The zone of larger growth lengths (L_g>60) is colored in light gray and a double black line marks Dθ=1.5. As a consequence, the objective (L_g≤60 and Dθ≥1.5) is achieved in a restricted zone around Re=155 and f_{exc}=0.17.

For this purpose, an additional simulation has been performed at Re=150, ε=3.5, f_{exc}=0.17 and A_{exc}=2. This case is numbered #32 in Table 1 and the associated results are included in Table 3 of Appendix C. The instantaneous temperature field at z=0.5 and a series of velocity vector and temperature fields in the vertical transverse plane at x=139 are presented in Figures 15 and 16 for the fully-developed regime. It appears that the growth

length of the wavy rolls is rather short and their spanwise oscillations are well amplified in the channel core: $L_g=57.5$ and $D\theta=1.50$ which confirms the prediction obtained by the response surface. On the other hand, the oscillation magnitude is very small near the walls due to the lateral confinement.
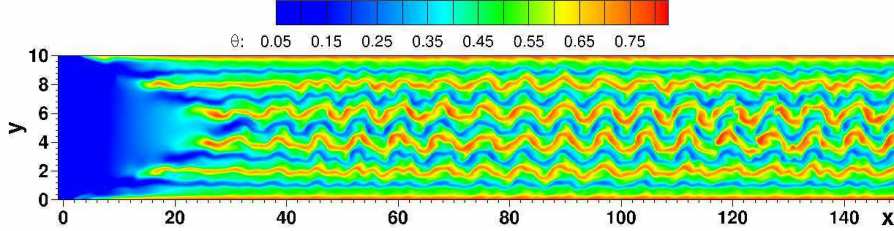

FIG. 15: Instantaneous temperature field in the horizontal mid-plane at $z=0.5$ in the fully-developed wavy roll flow at Re=150, $\varepsilon=3.5$, $f_{exc}=0.17$ and $A_{exc}=2$ (case #32).
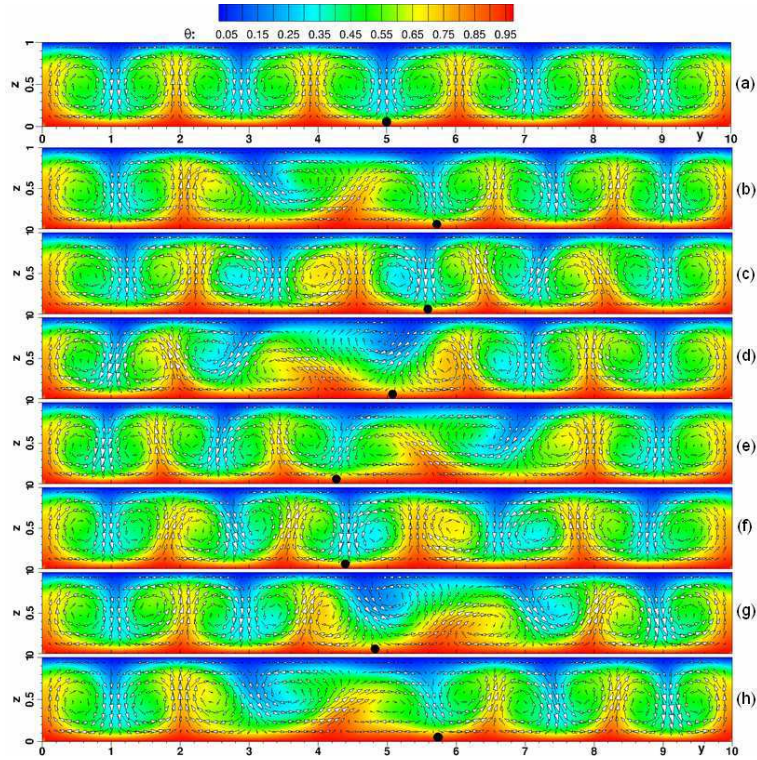
FIG. 16: Instantaneous velocity vector and temperature fields in the vertical plane at $x=139$, Re=150 and $\varepsilon=3.5$. Case (a) without excitation: ten steady longitudinal rolls are observed. Cases (b) to (h) with the inlet excitation defined by $f_{exc}=0.17$ and $A_{exc}=2$ (case #32): one period of the fully-developed wavy roll flow is observed with $\Delta t=1$ between each picture. A black point on the bottom plate indicates the location, y, of the impact of the downward cold jet of channel center. Starting from $y=5$ when the flow is steady (case (a)), the impact position moves from $y=4.25$ to $y=5.75$ as the flow is wavy and unsteady (cases (b) to (h)).

Let's analyze now the consequence of the waviness on the heat transfer distribution on the bottom plate of the PRB channel. Fig. 17 shows that, in the case of steady longitudinal rolls (Fig. 17 (a)), the Nusselt number is very heterogeneous in the spanwise direction as longitudinal parallel ridges of high intensity are observed. In the case of wavy roll flows (Fig. 17 (b)), the time averaged Nusselt number, <Nu>, is much more uniform at center and in the downstream part of the channel, where the wavy rolls have the highest oscillation amplitude. This is clear in Fig. 18 where spanwise <Nu> profiles for the longitudinal and wavy rolls are compared for $0 \leq y \leq 5$ (the symmetry through the central vertical plane at y=5 is taken into account). For $x \leq 29$, both <Nu> profiles are similar because the longitudinal rolls are just fully developed. Indeed, by using a correlation established in [10], the growth length of the longitudinal rolls is $L_{R//}=25.6$ at Re=150 and Ra=14575. On the other hand, the magnitude of the spanwise <Nu> oscillations is divided by two or more for the wavy rolls, compared with the fully developed longitudinal rolls, when $x \geq L_g=57.5$ and $3<y<7$; <Nu> is even nearly uniform for x>90 and $3.5 \leq y \leq 6.5$.
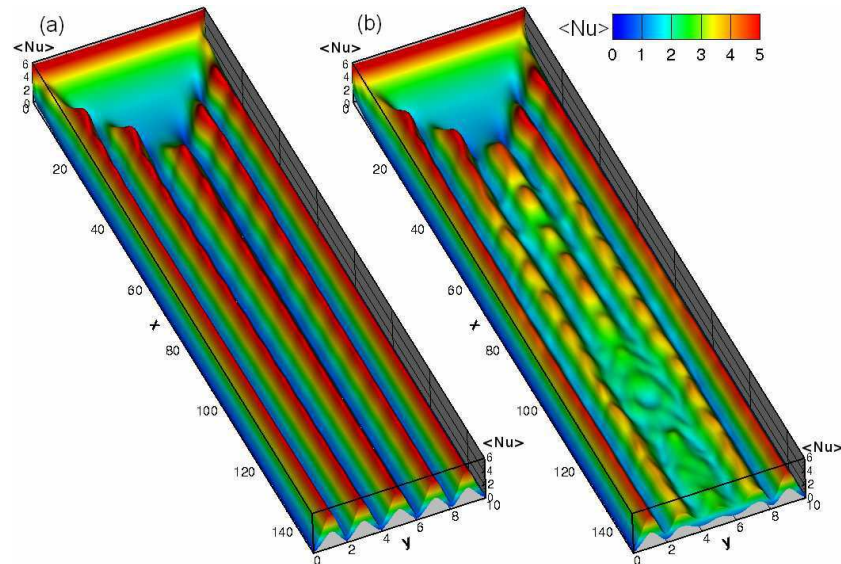

FIG. 17: Three dimensional surfaces of the time averaged local Nusselt numbers, <Nu>, on the bottom plate of the PRB channel: (a) steady longitudinal roll flow at Re=150, $\varepsilon=3.5$, $f_{exc}=0$ and $A_{exc}=0$; (b) wavy roll flow at Re=150, $\varepsilon=3.5$, $f_{exc}=0.17$ and $A_{exc}=2$ (case #32).
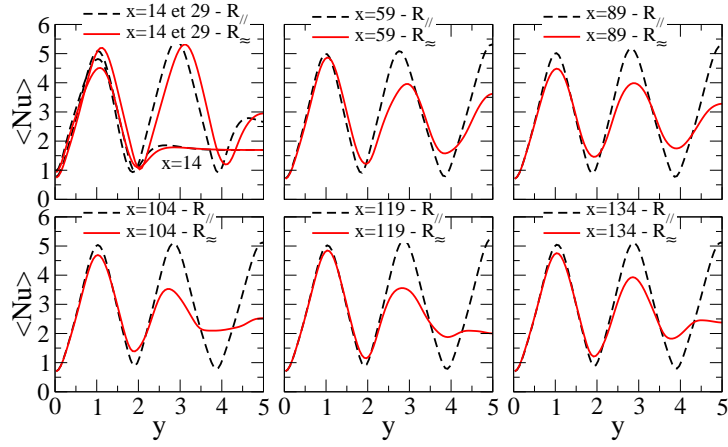
FIG. 18: Half spanwise profiles of the time averaged local Nusselt number, <Nu>, on the heated bottom plate for different streamwise coordinates, in the case of a steady longitudinal roll flow ($R_{//}$) at Re=150 and ε=3.5 (Fig. 17(a)) and for the associated wavy roll flow ($R_{\approx}$) at f_{exc}=0.17 and A_{exc}=2 (case #32 of Fig. 17(b)).

5.5. Average heat transfer intensity at saturation on the horizontal plates

In this section, we focus on the heat transfer intensity on the horizontal walls. Fig. 19 illustrates the streamwise variation of the spanwise averaged Nusselt number, $\overline{Nu}$ (x; z=0 or 1) (see Eq. (12)) in case #32 of Table 1. The magnitude of the Nusselt number oscillation is nearly the same on the top and bottom plates for $x \geq L_g$. As a consequence, the space and time averaged Nusselt number in the fully-developed region, $\overline{Nu}_{fd}$, is constant and has nearly equal values on the top and bottom plates. The intensity of heat transfer on the horizontal walls is therefore analyzed now from the response surface of $\overline{Nu}_{fd}$.

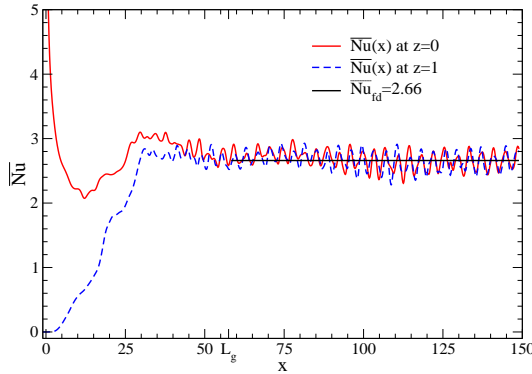FIG. 19: Streamwise profiles of the instantaneous and spanwise averaged Nusselt numbers on the horizontal walls ($\overline{Nu}$ (x; z=0 or 1)) and space and time averaged Nusselt number in the fully-developed region ($\overline{Nu}_{fd}$) at Re=150, ε=3.5, f_{exc}=0.17 and A_{exc}=2 (case #32 of Table 1).

33

The simplified response surface of $\overline{\mathrm{Nu}}_{fd}$ in the case of wavy rolls generated by harmonic excitations is (see also Eq. (35) of Appendix 2):

$$\overline{\mathrm{Nu}}_{fd} = 3.8941 - 0.019453\ \mathrm{Re} + 20.49352\ \varepsilon - 16.9125\ f_{exc} + 0.000086848\ \mathrm{Re}^2 - 0.017167$$

$$\varepsilon^2 + 89.0432\ f_{exc}^2 - 0.000000121545\ \mathrm{Re}^3 - 139.49268\ f_{exc}^3 - 0.00032852\ \mathrm{Re}\ \varepsilon +$$

$$0.0069023\ f_{exc}\ \mathrm{Re} - 0.623136\ f_{exc}\ \varepsilon \tag{17}$$

$$R^2=0.988;\ R_a^2=0.982;\ F=148.4;\ RMSE=0.027;\ Mean=2.405$$

Note that $\overline{\mathrm{Nu}}_{fd}$ is independent of A_{exc}. Its partial representation in Fig. 20 indicates that $\overline{\mathrm{Nu}}_{fd}$ is minimum for Re values between about 150 and 170 and increases mainly with ε and, to a lesser extent, with f_{exc}. The cube plot displayed in Fig. 20 (b) also indicates that $\overline{\mathrm{Nu}}_{fd}$ approximately varies between 1.9 and 2.9 in the studied parameter domain.
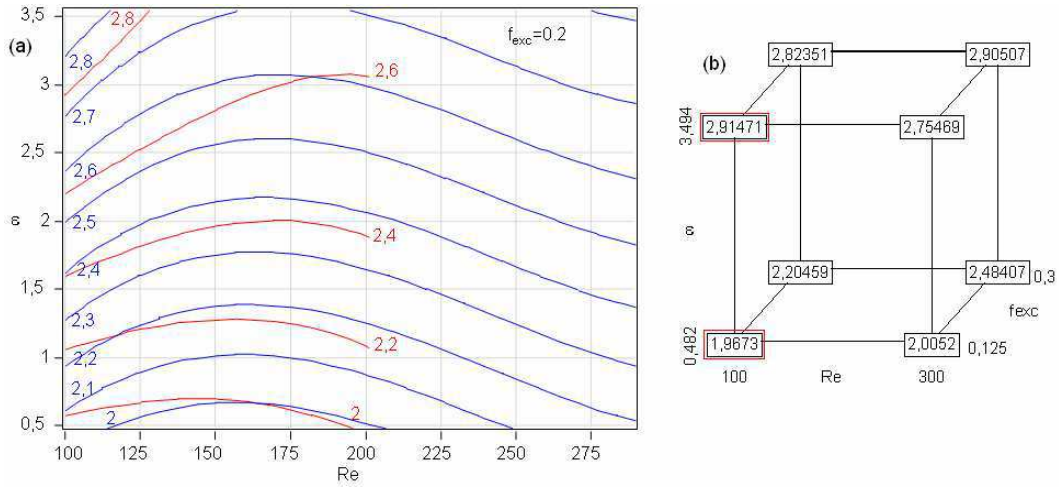

FIG. 20: Representations of the $\overline{\mathrm{Nu}}_{fd}$ response surface (Eq. (17)) as a function of Re, ε and f_{exc}: (a) Isocontours of $\overline{\mathrm{Nu}}_{fd}$ in the (Re, ε) plane: in blue, for $100 \le Re < 300$, case of the present wavy rolls at $f_{exc}=0.2$; in red, for $100 \le Re \le 200$, case of wavy rolls excited by a white noise (Eq. (18) from [10]). (b) Cube plots of $\overline{\mathrm{Nu}}_{fd}$ (see Fig. 13 for indications); red boxed values are the minimum and maximum of $\overline{\mathrm{Nu}}_{fd}$ on the vertices of the cube.

In Fig. 20(a), the $\overline{\mathrm{Nu}}_{fd}$ values computed from Eq. (17) at $f_{exc}=0.2$ are compared with the quadratic response surface established in [10] in the case of wavy rolls excited by a white

noise at channel inlet. This response surface, valid for $100 \leq Re \leq 200$ and $4500 \leq Ra \leq 15,000$ $(0.5 \leq \varepsilon \leq 3.5)$, writes:

$$\overline{Nu}_{fd} = (2172.2 - 7.145Re + 591.9\varepsilon + 0.0276Re^2 - 39.5\varepsilon^2 - 1.125\varepsilon Re) \times 10^{-3} \qquad (18)$$

It is independent on A_{exc} like Eq. (17) and also on f_{exc} since the used random excitation embraces all the frequencies. When similar figures as Fig. 20(a) are plotted for different values of f_{exc} in Eq. (17) (not shown here), it is interesting to observe that the best agreement of $\overline{Nu}_{fd}$ between the two studies with random and harmonic excitations is achieved for harmonic excitations at $f_{exc} \approx 0.2$. This approximately corresponds to the most amplified modes, $f°$, observed with a white noise since they are $f° \approx 0.22 \pm 0.04$ when $100 \leq Re \leq 200$ and $0.5 \leq \varepsilon \leq 3.5$ [10].

Finally, to sum up the results around the optimum point (case #32), Fig. 21 compares the behaviors of L_g, $\overline{Nu}_{fd}$ and $D\theta$ as a function of the flow parameters. These profiles are here computed from the full cubic response surfaces of L_g, $\overline{Nu}_{fd}$ and $D\theta$, without any simplification. One can note that the three quantities are nearly independent of A_{exc}. Furthermore a short growth length (small L_g) and a high heat transfer (large $\overline{Nu}_{fd}$) and a uniform heat transfer (large $D\theta$) can be reached by simply increasing ε. Unfortunately, these three objectives cannot be satisfied at the same time when Re and f_{exc} vary. In particular the maximum of $D\theta$ as a function of Re is obtained for $120 \leq Re \leq 150$ (see Figs. 12, 14 and 21) associated with a minimum of $\overline{Nu}_{fd}$ obtained for $150 \leq Re \leq 175$ (see Figs. 20 and 21). Thus, contrary to what could be thought at first, increasing the spanwise displacement of the wavy rolls does not allow an increase of the average heat transfer but rather a slight decrease of it. This has already been analyzed in [10] and is confirmed here: when $D\theta$ increases, the mixing of the flow in the channel core increases and its time averaged temperature is more uniform resulting in slightly smaller mean temperature gradients at walls (see [10] for more details). This decrease of $\overline{Nu}_{fd}$ with the magnitude of the spanwise oscillations of the wavy rolls is

also visible in Fig. 18. Indeed, in the $\overline{Nu}_{fd}$ profiles at x=104, 119 and 134, it clearly appears that the spanwise averaged Nusselt number in the longitudinal roll flow is higher than the spanwise averaged Nusselt number in the fully amplified wavy roll flow (for 3.5≤y≤5). Therefore, when choosing the Reynolds number, a compromise has to be found between more uniform and more intense heat transfers.

In the same way, when choosing the excitation frequency, a compromise has to be found between a shorter growth length of the wavy rolls and more uniform heat transfers. Indeed, Fig. 21 shows that the minimum (resp. maximum) of L_g with respect to f_{exc} is associated with the minimum (resp. maximum) of Dθ.
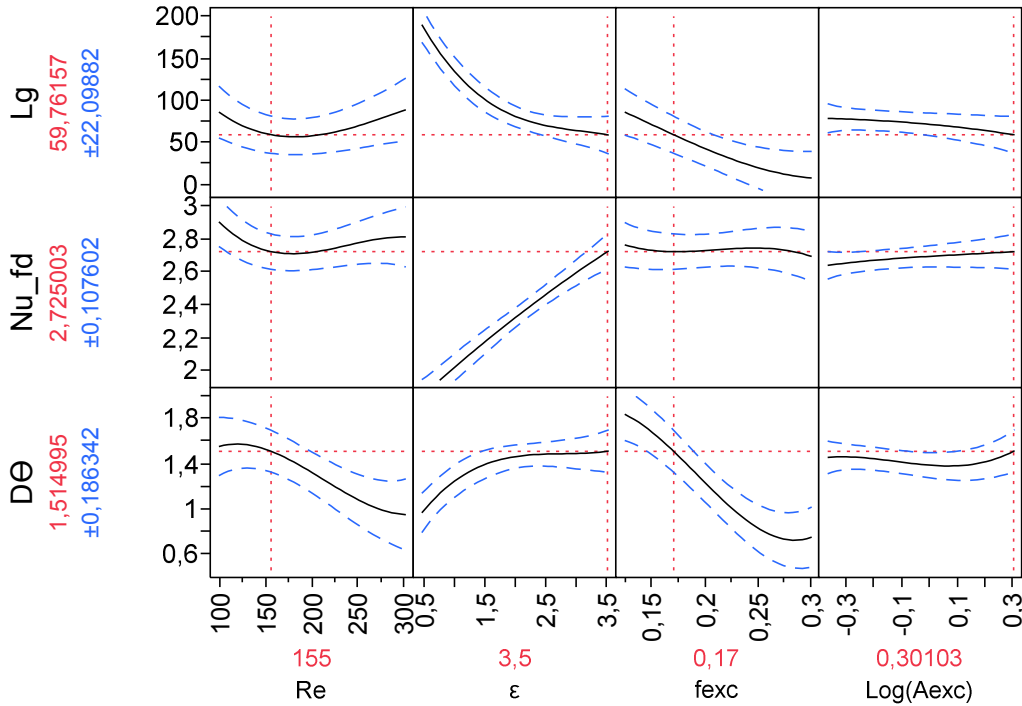
FIG. 21: Profiles of L_g, $\overline{Nu}_{fd}$ and Dθ as a function of Re, ε, f_{exc} and $Log(A_{exc})$, around the point Re=155, ε=3.5, f_{exc}=0.17 and A_{exc}=2 (case #32).

6. Conclusion and discussion from the point of view of CVD applications

In this paper, a control of the non uniform heat transfers resulting from the onset of steady longitudinal thermoconvective rolls in the PRB configuration has been proposed. It consists in exciting the longitudinal roll flows at channel inlet by introducing a harmonic

mechanical excitation in the velocity profile. This permanent excitation enables to amplify and maintain an unsteady convective instability of the longitudinal rolls that takes the form of wavy rolls. This unsteady pattern then provides more uniform time averaged heat transfers.

A numerical Design Of Experiments (DOE) has been built to analyze about ten responses characterizing the global structure and the heat transfers associated with the wavy thermoconvective flows at Pr=0.71, in channels of spanwise aspect ratio B=W/H=10, on a wide range of four parameters: for $100 \leq Re \leq 300$, $5000 \leq Ra \leq 16000$, $0.125 \leq f_{exc} \leq 0.3$ and $0.4 \leq A_{exc} \leq 2$. The studied responses are the wavy roll growth lengths until saturation (L_g, $L_\theta(f_0)$, $L_\theta(f_1)$), the magnitude of the most amplified modes in temperature spectra at different positions ($\bar{A}_\theta(f_0)$, $\bar{A}_\theta(f_1)$), the magnitude of the spanwise displacement of the wavy rolls in the channel core ($D\theta$), their spanwise wavelength (λ_y) and the average Nusselt number in the fully-developed zone ($\overline{Nu}_{fd}$).

The DOE has been built carefully and the statistical tests to determine the quality of the interpolations have been systematically checked in order to provide reliable polynomial response surfaces. The built response surfaces being quadratic or cubic functions of the flow and excitation parameters, they are very simple to manipulate and the behavior of the wavy rolls can be analyzed very easily on the wide parameter domain.

The numerical results obtained directly from DNS and DOE have been compared with the PRB experiments performed at FAST laboratory (Orsay, France) in which the wavy rolls are generated by the same type of harmonic mechanical excitation at channel inlet as in the numerical simulations. A very good agreement is observed concerning the growth length of the wavy rolls until saturation. A good agreement is also obtained concerning the spectral distribution of the amplified modes, but with a systematic gap between experiments and simulations, explained by the difficulty of controlling experimentally the position of the thermocouples relative to the wavy rolls.

All the studied responses characterizing the fully-developed wavy roll flows more or

less depend on Re, ε and f_{exc}. On the other hand, they are all independent or quasi independent of the excitation magnitude, A_{exc}, except the wavy roll growth length that (linearly) decreases as a function of $Log(A_{exc})$.

The joint analysis of the response surfaces of L_g and $D\theta$ has enabled to find the values of the flow and excitation parameters to simultaneously obtain small growth lengths and large oscillation magnitudes of the wavy rolls and, as a consequence, more uniform wall heat transfer in a large part of the channel. These conditions are obtained for moderate Reynolds number (Re≈150), high Rayleigh numbers (Ra≈15000), low excitation frequency (f_{exc}≈0.17) and rather high excitation magnitude (A_{exc}≈2). For these optimal conditions, it has been verified that more uniform time averaged Nusselt numbers are indeed observed on the horizontal walls for $x>L_g=60$ and in the channel core, because the vertical side walls of the rather narrow channel used prevent large oscillations nearby them. On the other hand, it has been shown that a compromise has to be done between more uniform and more intense heat transfer because $D\theta$ and $\overline{Nu}_{fd}$ have opposite behaviors with respect to Re.

We discuss now the results of the present work from the point of view of the application to the horizontal rectangular CVD reactors. The present study is a theoretical test case limited to laminar mixed convection flows in a quite narrow channel. In fact, there is a great multiplicity of operating conditions in CVD reactors. The flow regimes can be laminar or turbulent and can vary from forced convection flows at low Rayleigh numbers ($Ra<O(10^3)$) in the low pressure CVD reactors to mixed convection flows at very high Rayleigh numbers (until $Ra\sim O(10^6)$) in some APCVD reactors [2, 5]. Furthermore, some reactors are rather narrow and short with small spanwise and streamwise aspect ratios ($2\leq B=W/H<10$ and $A=L/H\sim O(10)$) such as those used for silicon deposition and electronic applications [3, 4]. Others can be very wide and long: for instance, the aspect ratios of the online APCVD reactors used to make depositions of metallic oxides on flat glass, in the float glass industry, are

generally larger than 100 and the spanwise aspect ratio can even reach 400 (the glass windows can measure four meter wide and the reactor height is around the centimeter [2, 34, 35]).

As a consequence, the fact that the lateral confinement prevent to make uniform heat (or mass) transfers on a distance equal to 2.5H from the vertical walls is not a drawback in some practical situations where channels or reactors of large spanwise aspect ratio are used. Indeed some CVD reactors are so wide that the influence of the lateral walls is negligible on the heat and mass transfer in the reactor core.

Another aspect of the discussion concerns the growth length of the thermoconvective patterns in the CVD processes. In the APCVD reactors, the temperature difference between the hot substrate and the cold ceiling of the reactor is important and the Rayleigh number can reach 10^5 or more. It is well known that the growth length of all the thermoconvective patterns in the PRB configuration decreases with increasing Rayleigh number when the other parameters are fixed (see §5.1 and [1, 6, 9, 10, 17, 21] for instance in the case of the transverse, longitudinal and wavy thermoconvective rolls). But, at Ra>10^5, it was also shown in [18, 32, 33] that a second type of initiation mechanism of the longitudinal rolls can appear at channel entrance, inducing very short growth lengths of the thermoconvective rolls for the same range of Reynolds numbers as in the present study. With this initiation mechanism two (or four) longitudinal rolls are symmetrically initiated along each vertical wall at channel entry and, at the same time, a Rayleigh-Bénard instability mechanism produces thermal plumes at the same axial coordinate, in the bottom thermal boundary layer, in the channel core. This initiation mechanism prevents the formation of the triangular forced convection zone that appears at lower Rayleigh numbers, visible in Figs. 4, 17 and 19. The development of wavy rolls and the characterization of the heat and mass transfers have never been studied in such a situation and it could be an interesting perspective for the present work.

Acknowledgements

Appendix A : Statistical tests and prediction variance

To evaluate the quality of the response surfaces presented in this paper, classical statistical tests of ANOVA (analysis of variance) have been computed. This appendix gives their definitions. Let y be the studied response and $(y_i)_{i=1,n}$ the n measurements of this response at the n points of the study domain (n=31 in the present work). Let $\hat{y}$ be the mathematical model of y and $(\hat{y}_i)_{i=1,n}$ the n values of this model at the same n points. In the present work, $\hat{y}$ is a polynomial response surface of p terms whose p coefficients are obtained by the least square method, with p=19 for the full cubic response surface given by Eq. (10). Finally let $(r_i)_{i=1,n} = (y_i - \hat{y}_i)_{i=1,n}$ be the errors or residuals at all points of the study domain. Then one can define:

- the global mean of the measured responses: $\text{MEAN} = \overline{y} = \dfrac{1}{n}\sum_{i=1}^{n} y_i$;

- the variance of the measured responses: $V(y) = \dfrac{1}{n-1}\sum_{i=1}^{n}(y_i - \overline{y})^2$;

- the variance of the model or of the computed responses: $V(\hat{y}) = \dfrac{1}{p-1}\sum_{i=1}^{n}(\hat{y}_i - \overline{y})^2$;

- the variance of the residuals or mean square error: $V(r) = \dfrac{1}{n-p}\sum_{i=1}^{n}(r_i)^2$;

- the root mean square error: $\text{RMSE} = \sqrt{V(r)} = \sqrt{\dfrac{1}{n-p}\sum_{i=1}^{n} r_i^2}$;

- the correlation coefficients: $R^2 = \dfrac{\sum_{i=1}^{n}(\hat{y}_i - \overline{y})^2}{\sum_{i=1}^{n}(y_i - \overline{y})^2} \leq 1$ and $R_a^2 = 1 - \dfrac{V(r)}{V(y)} \leq 1$;

-    the Fisher test: $F = \dfrac{V(\hat{y})}{V(r)}$.

A response surface is a good interpolation of the measurements if R^2 and R_a^2 are nearby 1 and F is much greater than 1. The 95% confidence interval of a response is the interval where there is a 95% chance to find the true response. This confidence interval depends on the variance of the coefficients of the postulated mathematical model which itself depends on the variance of the measured responses and RMSE. In the simple case of a full factorial design, the variance of the coefficients is proportional to the RMSE and to a coefficient that depends on the number n of measurements [26]. But, in a non conventional DOE as is the present one, a specialty software is necessary to make the calculation of the variance of the coefficients and of the 95% confidence intervals. In the present study, the response surface equations and all the statistical tests were computed using the DOE software JMP [31].

When doing a DOE, it is possible to compute a priori, before all experiment, the prediction variance. This function is the ratio of the variance of the response predicted by the model (by the response surface) to the variance of the measured response. The values of this function lower than one indicate the part of the study domain on which the prediction of the model is valid. Prediction variance profiles are plotted on Fig. 22 around the center of the study domain (case #1 of Table 1) and on Fig. 23 around the optimal point (case #32 of Table 1). It appears that the prediction variance is lower than one in most of the study domain. It strongly increases and can be larger than one only near the limits of the parameter domain but the prediction variance remains valid near the optimal point.
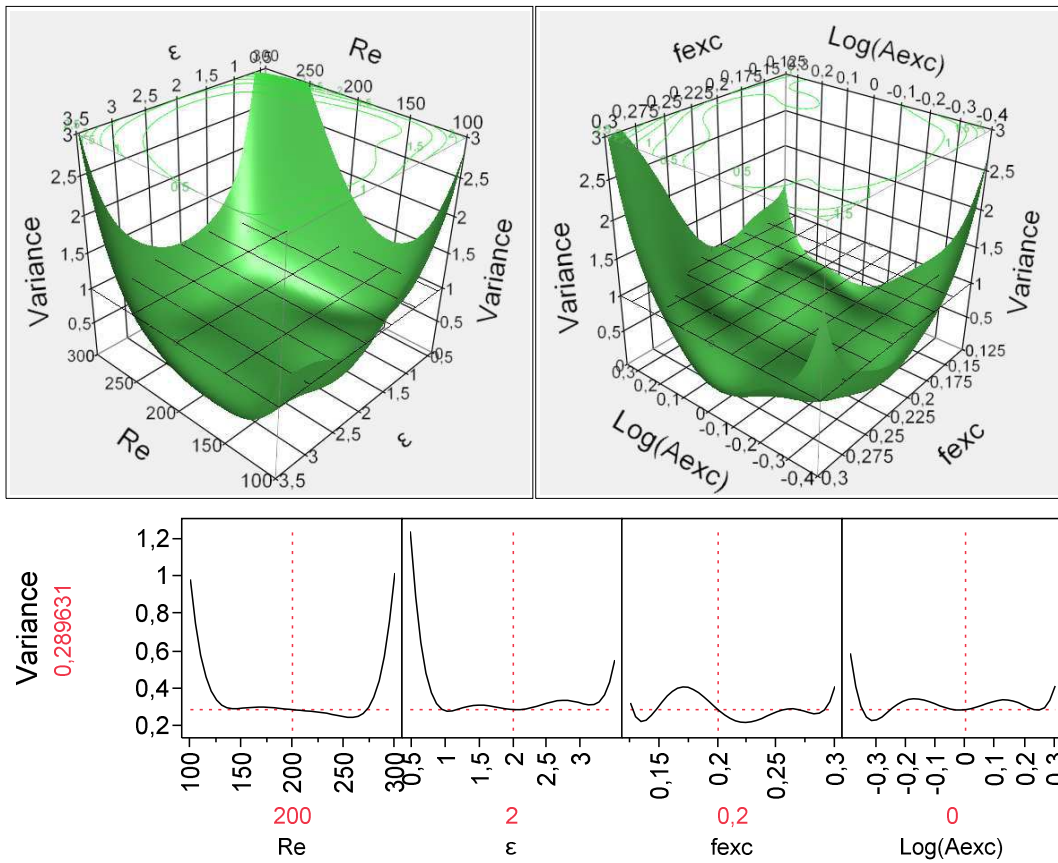
FIG. 22: Surface and profiles of the prediction variance function with respect to the flow parameters around the point Re=200, ε=2, f_{exc}=0.2 and A_{exc}=1 (nearby case #1 of Table 1).
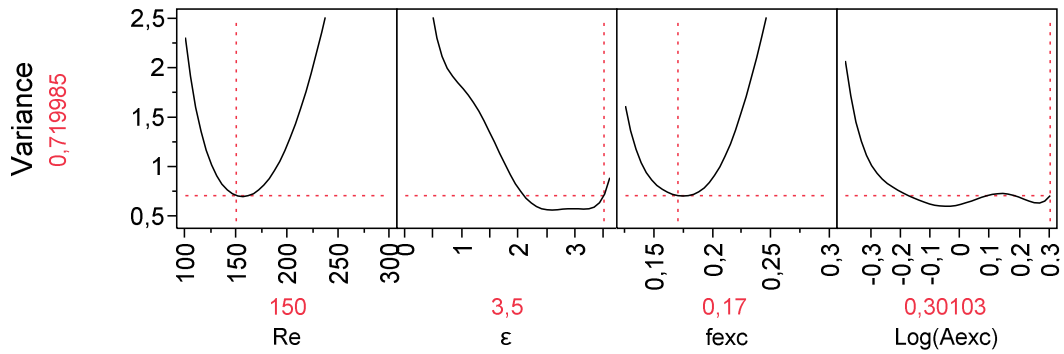

FIG. 23: Profiles of the prediction variance function with respect to the flow parameters around the point Re=150, ε=3.5, f_{exc}=0.17 and A_{exc}=2 (case #32 of Table 1).

Appendix B: Response surface equations

This appendix provides the simplified equations of all the response surfaces analyzed in this paper (except Eqs. (15-17)), in terms of the normal factors, x_i, and the centered and scaled factors, x_i', (see §3.2). It also provides the values of different statistical tests defined in Appendix A. All these tests certify the quality of the interpolations since, for most of the response surfaces, $R^2>0.98$, $R_a^2>0.96$ and $F>40$. The 31 first simulations of Table 1 are used to compute all the response surfaces, unless noted otherwise.

$$L_\theta(f_0) = 696.0247 - 403.8727\,(Re/Re^*) - 215.3178\,\varepsilon - 206.5564\,f_{exc} - 21.86075\,Log(A_{exc})$$
$$+ 120.5856\,(Re/Re^*)^2 + 65.04936\,\varepsilon^2 + 1098.7845\,f_{exc}^2 - 12.06144\,(Re/Re^*)^3 - 7.029342\,\varepsilon^3 +$$
$$18.77915\,(Re/Re^*)\,\varepsilon - 140.9255\,\varepsilon\,f_{exc} + 22.49143\,\varepsilon\,Log(A_{exc}) - 220.9749\,f_{exc}\,Log(A_{exc}) \quad (19)$$

$$L_\theta(f_0) = 68.33351 + 24.23996\,(Re/Re^*)' - 31.49747\,\varepsilon' - 0.895262\,f_{exc}' - 8.293909$$
$$Log(A_{exc})' + 38.86516\,(Re/Re^*)'^2 + 52.45449\,\varepsilon'^2 + 8.412569\,f_{exc}'^2 - 24.54239\,(Re/Re^*)'^3 -$$
$$24.01688\,\varepsilon'^3 + 35.84118\,(Re/Re^*)'\,\varepsilon' - 18.57227\,\varepsilon'\,f_{exc}' + 11.65731\,\varepsilon'\,Log(A_{exc})' - 6.653723$$
$$f_{exc}'\,Log(A_{exc})' \quad (20)$$

$$R^2=0.982;\ R_a^2=0.968;\ F=70.5;\ RMSE=5.34;\ Mean=88.57$$

$$L_\theta(f_1) = 629.7239 - 180.7396\,(Re/Re^*) - 169.6855\,\varepsilon - 1108.742\,f_{exc} + 187.8898\,Log(A_{exc})$$
$$+ 21.94402\,(Re/Re^*)^2 + 23.95543\,\varepsilon^2 + 2353.467\,f_{exc}^2 + 24.81971\,(Re/Re^*)\,\varepsilon + 84.97554$$
$$(Re/Re^*)\,f_{exc} - 33.19252\,(Re/Re^*)\,Log(A_{exc}) - 100.8250\,\varepsilon\,f_{exc} - 15.02282\,\varepsilon\,Log(A_{exc}) -$$
$$394.3169\,f_{exc}\,Log(A_{exc}) \quad (21)$$

$$L_\theta(f_1) = 69.53698 + 6.329706\,(Re/Re^*)' - 43.82713\,\varepsilon' - 5.743301\,f_{exc}' - 4.880657$$
$$Log(A_{exc})' + 35.23664\,(Re/Re^*)'^2 + 54.34237\,\varepsilon'^2 + 18.01873\,f_{exc}'^2 + 47.36998\,(Re/Re^*)'\,\varepsilon' +$$
$$9.421958\,(Re/Re^*)'\,f_{exc}' - 14.47415\,(Re/Re^*)'\,Log(A_{exc})' - 13.28751\,\varepsilon'\,f_{exc}' - 7.786325\,\varepsilon'$$
$$Log(A_{exc})' - 11.87319\,f_{exc}'\,Log(A_{exc})' \quad (22)$$

$$R^2=0.980;\ R_a^2=0.965;\ F=65.4;\ RMSE=5.44;\ Mean=92.63$$

$$\bar{A}_\theta(f_0)\ \text{at}\ y\approx B/2\text{-}0.5\ \text{computed without case \#11} = 3.897247 + 0.002883855\,Re +$$
$$0.0990001\,\varepsilon - 103.9990\,f_{exc} + 0.1019505\,Log(A_{exc}) - 1.789214\times10^{-5}\,Re^2 - 0.04554606\,\varepsilon^2 +$$
$$1049.295\,f_{exc}^2 + 0.02921743\,Log(A_{exc})^2 + 2.732254\times10^{-8}\,Re^3 + 0.006099978\,\varepsilon^3 - 5142.170$$
$$f_{exc}^3 + 12174.71\,f_{exc}^4 - 11193.94\,f_{exc}^5 + 0.003435454\,Re\,f_{exc} - 0.0005269348\,Re\,Log(A_{exc}) +$$
$$0.03642383\,\varepsilon\,f_{exc} \quad (23)$$

$\bar{A}_\theta(f_0)$ at y≈B/2-0.5 computed without case #11 = 0.1178183 - 0.02415546 Re' - 0.003057056 ε' - 0.06300225 f_{exc}' - 0.002049106 Log(A_{exc})' - 0.01498615 Re'^{2} - 0.02078617 ε'^{2} - 0.03360801 f_{exc}'^{2} + 0.003459949 Log(A_{exc})'^{2} + 0.02732254 Re'^{3} + 0.02084156 ε'^{3} + 0.1015424 f_{exc}'^{3} + 0.01648062 f_{exc}'^{4} - 0.05741478 f_{exc}'^{5} + 0.03006022 Re' f_{exc}' - 0.01813304 Re' Log(A_{exc})' + 0.004800218 ε' f_{exc}' (24)

R^2=0.982; R_a^2=0.959; F=43.9; RMSE=0.0039; Mean=0.1093 (without case #11)

$\bar{A}_\theta(f_1)$ at y=B/2 = -1.143385 + 0.001879925 Re + 0.1007241 ε + 21.33103 f_{exc} - 1.184232×10^{-5} Re^2 - 0.0638189 ε^2 - 152.2703 f_{exc}^2 + 1.83499×10^{-8} Re^3 + 0.0093640 ε^3 + 452.0639 f_{exc}^3 - 488.6181 f_{exc}^4 + 9.70967×10^{-5} Re ε + 0.001184152 Re f_{exc} - 0.0002568074 Re Log(A_{exc}) + 0.09477817 ε f_{exc} - 0.01190459 ε Log(A_{exc}) + 0.3636938 f_{exc} Log(A_{exc}) (25)

$\bar{A}_\theta(f_1)$ at y=B/2 = 0.05475080 - 0.0196806 Re' - 0.002453063 ε' - 0.04287955 f_{exc}' - 0.00854033 Re'^{2} - 0.01795359 ε'^{2} + 0.02473988 f_{exc}'^{2} + 0.0180447 Re'^{3} + 0.03114458 ε'^{3} + 0.02457169 f_{exc}'^{3} - 0.02627256 f_{exc}'^{4} + 0.01422482 Re' ε' + 0.01044974 Re' f_{exc}' - 0.008866129 Re' Log(A_{exc})' + 0.01256749 ε' f_{exc}' - 0.006048305 ε' Log(A_{exc})' + 0.01086985 f_{exc}' Log(A_{exc})' (26)

R^2=0.977; R_a^2=0.952; F=37.9; RMSE=0.00392; Mean=0.05273

$\bar{A}_\theta(f_0)$ at y≈B/2-0.33 computed without case #11 = 5.895955 + 0.001449948 Re + 0.02965187 ε - 157.7524 f_{exc} + 0.01002236 Log(A_{exc}) - 9.390035×10^{-6} Re^2 - 0.024260 ε^2 + 1633.919 f_{exc}^2 + 0.0352445 Log(A_{exc})^2 + 1.423205×10^{-8} Re^3 + 0.003031883 ε^3 - 8206.292 f_{exc}^3 + 19985.991 f_{exc}^4 - 18949.155 f_{exc}^5 + 6.17380×10^{-5} Re ε + 0.001515424 Re f_{exc} + 0.07716775 ε f_{exc} (27)

$\bar{A}_\theta(f_0)$ at y≈B/2-0.33 computed without case #11 = 0.08877126 - 0.01534488 Re' - 0.003184832 ε' - 0.05713407 f_{exc}' + 0.002403622 Log(A_{exc})' - 0.008508074 Re'^{2} - 0.01401116 ε'^{2} - 0.007217776 f_{exc}'^{2} + 0.004173679 Log(A_{exc})'^{2} + 0.01423205 Re'^{3} + 0.01035892 ε'^{3} + 0.1507814 f_{exc}'^{3} - 0.008645341 f_{exc}'^{4} - 0.097191978 f_{exc}'^{5} + 0.009298649 Re' ε' + 0.01325996 Re' f_{exc}' + 0.01016977 ε' f_{exc}' (28)

R^2=0.959; R_a^2=0.909; F=19.0; RMSE=0.00347; Mean=0.08254

$\bar{A}_\theta(f_1)$ at y=B/2-0.33 = -0.5674319 + 0.002841371 Re + 0.06129390 ε + 10.36498 f_{exc} - 0.1022064 Log(A_{exc}) - 1.608725×10^{-5} Re^2 - 0.03419296 ε^2 - 89.97388 f_{exc}^2 - 0.04056966 Log(A_{exc})^2 + 2.61366×10^{-8} Re^3 + 0.004789451 ε^3 + 315.7115 f_{exc}^3 - 0.2916017 Log(A_{exc})^3 - 398.2689 f_{exc}^4 + 0.001319137 Re f_{exc} - 0.0003543790 Re Log(A_{exc}) + 0.07738846 ε f_{exc} - 0.008503581 ε Log(A_{exc}) + 0.9657349 f_{exc} Log(A_{exc}) (29)

44

$\bar{A}_\theta(f_1)$ at $y=B/2-0.33 = 0.03588318 - 0.01615449$ Re' $- 0.001599074$ ε' $- 0.001355596$ f_{exc}' $+ 0.005885233$ Log(A_{exc})' $- 0.004052689$ Re'$^2 - 0.01276364$ ε'$^2 + 0.02592563$ f_{exc}'$^2 - 0.0003400595$ Log(A_{exc})'$^2 + 0.02613663$ Re'$^3 + 0.01636394$ ε'$^3 - 0.01528566$ f_{exc}'$^3 - 0.01188315$ Log(A_{exc})'$^3 - 0.02334579$ f_{exc}'$^4 + 0.01154245$ Re' f_{exc}' $- 0.01219499$ Re' Log(A_{exc})' $+ 0.01019886$ ε' f_{exc}' $- 0.004407405$ ε' Log(A_{exc})' $+ 0.02907902$ f_{exc}' Log(A_{exc})'   (30)

$R^2=0.965$; $R_a{}^2=0.912$; F=18.2; RMSE=0.0036; Mean=0.0348

$D\theta = -1.756986 + 0.01947727$ Re $+ 0.9587349$ ε $+ 35.75977$ f_{exc} $- 0.2274313$ Log(A_{exc}) $- 1.225783×10^{-4}$ Re$^2 - 0.3528563$ ε$^2 - 245.9273$ $f_{exc}{}^2 + 1.091683$ Log(A_{exc})$^2 + 1.927105×10^{-7}$ Re$^3 + 0.04271694$ ε$^3 + 421.0985$ $f_{exc}{}^3 + 3.377437$ Log(A_{exc})$^3 + 0.01602055$ Re f_{exc} (31)

$D\theta = 0.8510430 - 0.3024399$ Re' $+ 0.09371140$ ε' $- 0.7445842$ f_{exc}' $- 0.1041672$ Log(A_{exc})' $- 0.06951943$ Re'$^2 - 0.2224772$ ε'$^2 + 0.1724416$ f_{exc}'$^2 + 0.07757151$ Log(A_{exc})'$^2 + 0.1927105$ Re'$^3 + 0.1459493$ ε'$^3 + 0.2821031$ f_{exc}'$^3 + 0.1376349$ Log(A_{exc})'$^3 + 0.1401798$ Re' f_{exc}'   (32)

$R^2=0.989$; $R_a{}^2=0.980$; F=112.6; RMSE=0.049; Mean=0.918

$\lambda_y = 3.583701 + 0.007546033$ Re $+ 0.4677752$ ε $- 39.63022$ f_{exc} $- 1.982811$ Log(A_{exc}) $- 2.60769×10^{-5}$ Re$^2 - 0.1218955$ ε$^2 + 211.6004$ $f_{exc}{}^2 - 0.1686435$ Log(A_{exc})$^2 + 3.956629×10^{-8}$ Re$^3 + 0.02452726$ ε$^3 - 340.8219$ $f_{exc}{}^3 - 0.000794504$ Re ε $- 0.003694637$ Re f_{exc} $- 0.003170226$ Re Log(A_{exc}) $- 0.4836759$ ε f_{exc} $+ 0.2552500$ ε Log(A_{exc}) $+ 8.663484$ f_{exc} Log(A_{exc})   (33)

$\lambda_y = 2.204498 - 0.03648678$ Re' $+ 0.001882916$ ε' $+ 0.1798423$ f_{exc}' $- 0.08735758$ Log(A_{exc})' $- 0.02337144$ Re'$^2 + 0.05534188$ ε'$^2 - 0.04343834$ f_{exc}'$^2 - 0.01997088$ Log(A_{exc})'$^2 + 0.03956629$ Re'$^3 + 0.08380133$ ε'$^3 - 0.2283241$ f_{exc}'$^3 - 0.1196640$ Re' ε' $- 0.03232808$ Re' f_{exc}' $- 0.1090948$ Re' Log(A_{exc})' $- 0.06374261$ ε' f_{exc}' $+ 0.1322960$ ε' Log(A_{exc})' $+ 0.2608642$ f_{exc}' Log(A_{exc})'   (34)

$R^2=0.992$; $R_a{}^2=0.983$; F=100.8; RMSE=0.015; Mean=2.184

$\overline{Nu}_{fd} = 2.406620 + 0.1515852$ Re' $+ 0.3421554$ ε' $+ 0.1901689$ f_{exc}' $+ 0.1388673$ Re'$^2 - 0.03912437$ ε'$^2 - 0.1217522$ Re'$^3 - 0.09328305$ f_{exc}'$^3 - 0.04956879$ Re' ε' $+ 0.06048041$ Re' f_{exc}' $- 0.08200362$ ε' f_{exc}'   (35)

$R^2=0.988$; $R_a{}^2=0.983$; F=171.8; RMSE=0.026; Mean=2.405

Appendix C: Values of the responses for all the DOE simulations

TAB. 3. Values of the measured responses for the 31 simulations of the DOE and for the optimal point case #32 (see the flow parameters in Table 1).

Case #	L_g	$L_\theta(f_1)$	$\bar{A}_\theta(f_0)$ at $y\approx B/2-0.5$	$\bar{A}_\theta(f_1)$ at $y=B/2$	$D\theta$	λ_y	$\overline{Nu}_{fd}$
1	88	78.2	0.1264	0.0635	0.90	2.165	2.385
2	117.2	104.1	0.1109	0.0486	0.75	2.165	2.538
3	107.7	88.1	0.1050	0.0674	0.807	2.241	2.749
4	83.7	64.4	0.1293	0.0669	1.10	2.379	2.693
5	114.6	104.4	0.1145	0.0551	1.00	2.149	2.515
6	193.4	182.4	0.0961	0.0305	0.598	2.057	1.929
7	130.8	132.2	0.0932	0.0311	0.556	2.166	2.271
8	76.8	85.7	0.0839	0.0321	0.469	2.057	2.699
9	62.4	59.8	0.0706	0.0349	0.566	2.166	2.565
10	146	145.1	0.0654	0.0165	0.395	2.167	2.281
11	116.5	121.7	0.1332	0.0581	1.20	2.167	2.190
12	120	127.3	0.1404	0.0879	1.605	2.113	2.154
13	120	92.5	0.1106	0.0550	1.45	2.248	2.602
14	61	60.8	0.0937	0.0408	0.674	2.117	2.604
15	67	58.4	0.1203	0.0578	0.981	2.279	2.502
16	113.1	120.1	0.0936	0.0340	0.59	2.111	2.206
17	87	82.4	0.1263	0.0720	1.40	1.943	2.271
18	105.9	108.5	0.1230	0.0586	1.049	2.332	2.277
19	97	90.2	0.1376	0.0777	1.20	2.230	2.203
20	89	65.7	0.1331	0.0738	1.20	2.279	2.530
21	77.5	77.7	0.0909	0.0369	0.62	2.190	2.477
22	69.6	59.6	0.1216	0.0600	0.998	2.276	2.501
23	120	113.7	0.1051	0.0395	0.655	2.040	2.170
24	90	94.2	0.1145	0.0740	1.551	1.834	2.330
25	82	81.4	0.1103	0.0486	0.787	2.223	2.404
26	78	78.2	0.1063	0.0482	0.787	2.241	2.406
27	77	71.2	0.1088	0.0491	0.795	2.240	2.404
28	107	103.2	0.1029	0.0408	0.713	2.298	2.275
29	99	97.7	0.1039	0.0416	0.719	2.277	2.275
30	56.5	53.8	0.0780	0.0441	0.737	2.279	2.759
31	78.5	68.4	0.1327	0.0896	1.60	2.278	2.402
32	*61.7*	*53.2*	*0.1389*	*0.0672*	*1.50*	*2.334*	*2.665*

References

[1] X. Nicolas, Bibliographical review on the Poiseuille-Rayleigh-Bénard flows: the mixed convection flows in horizontal rectangular ducts heated from below, Int. J. Thermal Sc., 41 (2002) 961-1016.

[2] X. Nicolas, A. Benzaoui, S. Xin, Numerical simulation of thermoconvective flows and more uniform depositions in a cold wall rectangular APCVD reactor, Journal Crystal Growth, 310 (2008) 174-186.

[3] H. K. Moffat, K. F. Jensen, Three-dimensional flow effects in silicon CVD in horizontal reactors, J. Electrochemical Society, 135 (1988) 459-470.

[4] C. R. Kleijn, C. J. Hoogendoorn. A study of 2-D and 3-D transport phenomena in horizontal chemical vapor deposition reactor, Chemical Engineering Science, 46 (1991) 321-334.

[5] R. L. Mahajan, Transport phenomena in chemical vapor deposition systems, Adv. Heat Trans., 28 (1996) 339-415.

[6] M. T. Ouazzani, J. K. Platten, A. Mojtabi, Etude expérimentale de la convection mixte entre deux plans horizontaux à températures différentes – 2, Int. J. Heat Mass Transfer, 33 (1990), 1417–1427.

[7] C. H. Yu, M. Y. Chang, T. F. Lin, Structures of moving transverse and mixed rolls in mixed convection of air in a horizontal plane channel, Int. J. Heat Mass Transfer, 40 (1997) 333–346.

[8] R. M. Clever, F. H. Busse, Instabilities of longitudinal rolls in the presence of Poiseuille flow, J. Fluid Mech., 229 (1991) 517-529.

[9] X. Nicolas, J. M. Luijkx, J. K. Platten, Linear stability of mixed convection flows in horizontal rectangular channels of finite transversal extension heated from below, Int. J. Heat Mass Transfer, 43 (2000) 589-610.

[10] X. Nicolas, N. Zoueidi, S. Xin, Influence of a white noise at channel inlet on the parallel and wavy convective instabilities of Poiseuille-Rayleigh-Bénard flows. Phys. Fluids, 24 (2012) 084101.

[11] A. Barletta, D. A. Nield, On the Rayleigh-Bénard-Poiseuille problem with internal heat generation, Int. J. Thermal Sc., 57 (2012) 1-16.

[12] C. Jung, M. Lücke, P. Büchel, Influence of through-flow on linear pattern formation properties in binary mixture convection, Phys. Rev. E, 54 (1996) 1510-1529.

[13] P. Büchel, M. Lücke, Influence of through flow on binary fluid convection, Phys. Rev. E, 61 (2000) 3793-3810.

[14] H. Ben Hamed, R. Bennacer, T. Langlet, H. Samouda, H. Béji, Numerical 3-D study of Poiseuille Rayleigh Benard Soret problem in a finite extent paralellipipedic duct, Num. Heat Transf. A, 55 (2009) 534-552.

[15] O. Rahli, R. Bennacer, K. Bouhadef, D. E. Ameziani, Three-dimensional mixed convection heat and mass transfer in a rectangular duct: case of longitudinal rolls, Num. Heat Transf. A, 59 (2011) 349–371.

[16] P. Carrière, P. A. Monkewitz, Convective versus absolute instability in mixed Rayleigh-Bénard-Poiseuille convection, J. Fluid Mech., 384 (1999) 243-262.

[17] S. Mergui, X. Nicolas, S. Hirata, Sidewall and thermal boundary conditions effect on the evolution of longitudinal rolls in Rayleigh-Bénard-Poiseuille convection. Phys. of Fluids 23 (2011) 084101.

[18] A. Benderradji, A. Haddad, R. Taher, M. Medale, C. Abid, F. Papini, Characterization of fluid flow patterns and heat transfer in horizontal channel mixed convection, Heat Mass Trans., 44 (2008) 1465-1476.

[19] S. Xin, X. Nicolas, P. Le Quéré, Stability analyses of longitudinal rolls of Poiseuille-Rayleigh-Bénard flows in air-filled channels of finite transversal extension, Num. Heat Trans. A, 50 (2006) 467-490.

[20] Y. Kato, K. Fujimura, Prediction of three-dimensional breakdown of a longitudinal roll in a square duct, The 50th Japan Natl. Congress on Theoretical and Applied Mechanics, 50 (2001) 327–333.

[21] H. Pabiou, S. Mergui, C. Bénard, Wavy secondary instability of longitudinal rolls in Rayleigh-Bénard-Poiseuille flows, J. Fluid Mech., 542 (2005) 175-194.

[22] A. Benzaoui, X. Nicolas, S. Xin, Efficient vectorized finite difference method to solve the incompressible Navier-Stokes equations for 3D mixed convection flows in high aspect ratio channels, Num. Heat Trans. B, 48 (2005) 277-302.

[23] F. Seychelles, S. Mergui, X. Nicolas, Experimental and numerical study on the wavy instability in a Rayleigh-Bénard-Poiseuille flow: non linear effects, J. Phys.: Conf. Series, 395 (2012) 012101.

[24] F. Seychelles, S. Mergui, Experiments on the wavy instability in Rayleigh-Bénard-Poiseuille convection: spatial and temporal features in the nonlinear regime, submitted to Int. J. Heat Fluid Flow (2013).

[25] X. Nicolas, M. Medale, S. Glockner, S. Gounand, Benchmark solution for a three-dimensional mixed convection flow – Part 1: reference solutions, Num. Heat Transfer B, 60 (2011) 325-345.

[26] J. Goupy, L. Creighton, Introduction to design of experiments with JMP examples, 3rd ed., SAS Press Series, SAS Institute Inc., Cary, NC, USA (2007).

[27] W. K. S. Chiu, Y. Jaluria and G. N. Glumac, Numerical simulation of chemical vapor deposition processes under variable and constant property approximations, Num. Heat Trans. A, 37 (2000) 113-132.

[28] Q. Wang, H. Yoo, Y. Jaluria, Convection in a horizontal rectangular duct under constant and variable property formulations, Int. J. Heat Mass Trans., 46 (2003) 297-310.

[29] H. W. Müller, M. Lücke, M. Kamps, Transversal convection patterns in horizontal shear flow, Phys. Rev. A, 45 (1992) 3714-3725.

[30] M. Westerburg, F. H. Busse, Finite-amplitude convection in the presence of finitely conducting boundaries, J. Fluid Mech., 432 (2001) 351-367.

[31] JMP, Version 9, SAS Institute Inc., Cary, NC, USA (2010).

[32] F. P. Incropera, A. L. Knox, J. R. Maughan, Mixed-Convection flow and heat transfer in the entry region of a horizontal rectangular duct, J. Heat Transfer, 109 (1987) 434-439.

[33] C. Gau, C. W. Liu, T. M. Huang, W. Aung, Secondary flow and enhancement of heat transfer in horizontal parallel-plate and convergent channels heating from below, Int. J. Heat Mass Trans., 42 (1999) 2629-2647.

[34] D.W. Sheel, M.E. Pemble, Atmospheric pressure CVD coatings on glass, Proceedings of the 4th International Conference for Coatings on Glass, Braunschweig, Germany, 2002.

[35] R. Gordon, Section 3. Glass coating at atmospheric pressure: Chemical vapor deposition of coatings on glass, J. Non-Cryst. Solids 218 (1997) 81-91